Solar-powered and antibacterial water purification via Cu-BTC-embedded reduced graphene oxide nanocomposite aerogels

Ahmad Allahbakhsh [1,2,*], Zeinab Jarrahi [1], Gholamali Farzi [1], Amin Shavandi [2,*]

[1] *Department of Materials and Polymer Engineering, Faculty of Engineering, Hakim Sabzevari University, Sabzevar, Iran*

[2] *Université libre de Bruxelles (ULB), École polytechnique de Bruxelles, 3BIO-BioMatter, Avenue F.D. Roosevelt, 50 - CP 165/61, 1050 Brussels, Belgium*

* *Corresponding authors. E-mail: a.allahbakhsh@hsu.ac.ir, ahmad.allahbakhsh@ulb.be (A. Allahbakhsh); amin.shavandi@ulb.be (A. Shavandi)*

The journal version is available at: https://doi.org/10.1016/j.cej.2023.143472

Abstract

Advancements in the design of porous active materials for interfacial solar evaporation have shown promise in the development of next-generation solar evaporation active materials that can present a wide range of water-purification properties. In this study, a new class of metal-organic nanoparticles-embedded reduced graphene oxide (rGO) nanocomposite aerogels is developed, with both solar steam generation behavior and antibacterial properties. The self-assembly process is used to introduce Cu-BTC nanoparticles (Cu-BTC NPs) into the structure of rGO aerogels to fabricate Cu-BTC/rGO nanocomposite aerogels. By varying the content of Cu-BTC NPs in the self-assembly precursor solution, the surface area, pore texture, and evaporation rate of samples are altered to reach both high energy conversion efficiency and

antibacterial properties. An evaporation rate of 1.13 kg/m^{2}h and an efficiency of 81.8% are achieved when the highest content of Cu-BTC NPs (1mg/ml) is introduced to the precursor solution. This evaporation efficiency is 32% and 59% higher than that of the rGO aerogel and pure water, respectively. This behavior is related to the surface area and pore size of the nanocomposite aerogels, which increase and decrease with the content of Cu-BTC NPs, respectively. Additionally, the Cu-BTC/rGO aerogel presents antibacterial activity against *S. aureus* and *E. coli*. As a result, Cu-BTC/rGO nanocomposite aerogels have great potential as active materials for the design of next-generation solar steam generation systems for the treatment of wastewater contaminated with pathogenic bacteria.

Keywords: solar steam generation, nanocomposite aerogels, interfacial evaporation, porous materials, graphene aerogels.

1. Introduction

Water and energy are two vital components of life that are essential for economic development and social progress [1]. However, with the development of modern societies, the availability of energy and water resources is increasingly threatened [2]. The rapid expansion of urbanization and industrialization has led to elevated levels of pollution, waste, and global warming, causing a critical level of clean water scarcity, especially in arid and semi-arid regions. To cope with these dilemmas, the scientific community has been encouraged to come up with solutions, particularly in the development of renewable and clean energy sources and the provision of clean water for all [3].

Solar-driven water treatment is an interesting approach that can provide a path to addressing the water scarcity crisis [4, 5]. This technique uses clean and renewable solar energy to generate steam from seawater, which is then condensed into fresh water, providing a sustainable and

effective approach to desalination [6]. However, this technology is still at an infant stage for large-scale applications, and the efficacy of solar steam generation systems is limited by a range of challenges, including irregular sunlight, complex fabrication protocols, salt accumulation, and biofouling [7]. To overcome these challenges, recent efforts have been focused on the development of novel active materials and structures with which the heat localization at the air/water interface can be optimized [8].

The solar energy harvesting performance of photothermal materials can be improved by tailoring their structural and morphological properties. This can be done by enhancing light trapping through design [9], increasing interfacial evaporation rate by adjusting the structure [10], and boosting solar absorption by using light-absorbing materials like carbon [11]. Using carbon-based porous materials, specifically graphene-based porous structures allows the structural design that combines these techniques, leading to improved performance in solar steam generation systems [12, 13].

Reduced graphene oxide (rGO) aerogels have been identified as a suitable candidate for the design of solar steam generation systems with broadband absorbance, chemical stability, high porosity, and partially reduced structure, resulting in hydrophilicity [14]. Furthermore, unlike traditional active materials, rGO aerogels have the potential to be converted into composites to offer a combination of water purification properties, such as solar steam generation and antibacterial properties [13], that can lead to the development of next-generation solar water purification systems. Metal-organic materials have also presented promising potential for the design of solar evaporation systems, considering their high porosity, high surface area, and structural tunability [15]. When metal-organic materials such as Cu-BTC nanorods are introduced into the structure of solar active materials, stable composite active materials with a high evaporation efficiency can be fabricated [16]. Moreover, our recent studies confirmed that

Cu-BTC nanoparticles (Cu-BTC NPs) have good antibacterial properties [17], making them a promising option for next-generation solar active materials.

The presence of pathogenic bacteria in wastewater can cause various health hazards, and removing them is necessary to make the water safe for reuse [18]. Antibacterial properties can be crucial in developing nanocomposite aerogels for solar steam generation applications as they can help in treating wastewater contaminated with pathogen bacteria. Moreover, when nanocomposite aerogels have anti-biofouling properties the lifetime of the final solar steam generation system can be longer, as the chance of biofouling and the closure of the water uptake channels in the structure of nanocomposite aerogels reduce significantly [19].

This study presents an innovative fabrication protocol for the design of next-generation antibacterial and anti-biofouling rGO-based solar evaporation active materials by ingeniously integrating Cu-BTC NPs, synthesized through a simple and fast solid-state solvosonication process, into rGO aerogel matrices. The incorporation of the solar absorption and evaporation capabilities of hydrophilic rGO aerogels with the antibacterial and anti-biofouling properties and porous structure of Cu-BTC NPs has led to the development of a solar steam generation system that not only boasts the efficiency of rGO aerogels but also possesses the added benefit of antibacterial and anti-biofouling properties within the Cu-BTC/rGO nanocomposite aerogels.

2. Experimental

2.1. Materials

Graphite powder was purchased from LECO. L-ascorbic acid was obtained from Acros Organics. All other chemicals, including sulfuric acid (H_2SO_4), potassium permanganate

($KMnO_4$), hydrogen peroxide (H_2O_2), hydrogen chloride (HCl), benzene tricarboxylic acid (BTC), copper acetate ($Cu(CH_3COO)_2 \cdot xH_2O$), dimethyl sulfoxide (DMSO), and N, N-dimethylformamide (DMF) were purchased from Merck Chemicals and used as received.

2.2. Preparation of Cu-BTC/rGO nanocomposite aerogels

Cu-BTC/rGO nanocomposite aerogels were fabricated using Cu-BTC NPs and GO nanosheets as precursors, following the procedure shown in **Figure 1**.

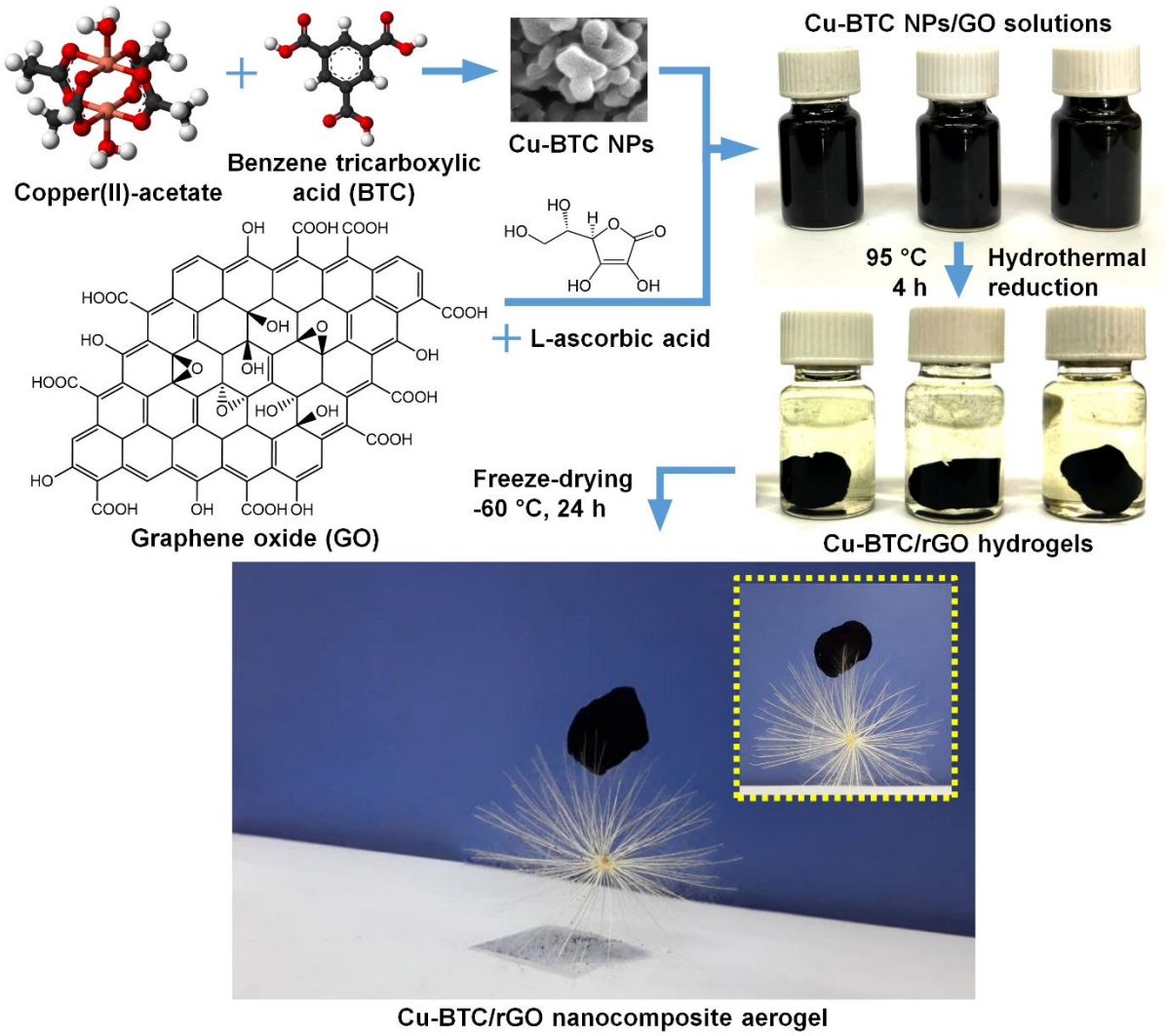

Figure 1. *Schematic of the protocol followed in this work for the fabrication of Cu-BTC/rGO nanocomposite aerogels*

***Synthesis of Cu-BTC NPs*:** Cu-BTC NPs were synthesized through the solvothermal process. A solution of 15 ml of DMF and 15 ml of distilled water was prepared and 0.105 g BTC and 0.199 g copper acetate were dissolved in them. The mixture was homogenized with an ultrasonic bath (Free 9 Tecno-Gaz,300 W, 50 Hz) for 45 min. The resulting Cu-BTC NPs were filtered, washed with DMF three times, dried, and used to prepare nanocomposite samples.

***Synthesis of GO nanosheets*:** Graphite was used as the precursor to synthesize GO nanosheets through a modified synthesis process [20]. Initially, 1 g of graphite was mixed with 100 mL of H_2SO_4 at room temperature, and $KMnO_4$ was gradually added as the oxidizer (6 g). The temperature of the solution during the $KMnO_4$ addition step was kept between 75–80 °C and the mixture was stirred for 4 hours. To dilute the oxidation solution, 300 mL of distilled water was added and mixed for 15 minutes. To terminate the oxidation reaction, 50 mL of H_2O_2 was added, and the dark product was washed with 10% HCl solution (5 times) and distilled water (5 times) via centrifugation. The obtained graphite oxide powder was then dispersed in distilled water using a Hielscher UP400S homogenizer (20 kHz, 400 W, 80% power), and the solution was centrifuged to remove graphite particles and undispersed aggregates, thereby obtaining a stable GO solution in water.

***Fabrication of Cu-BTC/rGO nanocomposite aerogels*:** Hydrogels and aerogels were prepared through the hydrothermal reduction of GO in the presence of Cu-BTC NPs in the precursor solution using l-ascorbic acid, followed by freeze-drying of hydrogels into aerogels. In a typical synthesis process, the Cu-BTC NPs powder was dispersed in distilled water using a Hielscher UP400S homogenizer (20 kHz, 400 W, 80% power). The stable solution of Cu-BTC NPs in water (ζ-potential: -30 mV, Figure S1) was added to the GO solution and the mixture was sonicated for 30 min. L-ascorbic acid with a ratio of 3 to 1 (concerning the GO content in the

solution) was added to the mixture and the mixture was stirred for 5 min. The solution was then sealed and placed in an electronic oven with a constant temperature of 95 °C for 4 h. Fabricated hydrogels were freeze-dried to nanocomposite aerogels using an ALPHA 1-2 LD plus laboratory freeze dryer at -55 °C for 24 h. Nanocomposite samples prepared in this study are listed in **Table 1**.

Table 1. *The fabrication conditions of Cu-BTC/rGO nanocomposite aerogels*

Sample	**Cu-BTC NPs content (mg/ml)**	**GO precursor solution concentration (mg/ml)**	**Hydrothermal reduction time (h)**
rGO-A	0	15	95
Cu-BTC/rGO-A-1	0.3	15	95
Cu-BTC/rGO-A-2	0.5	15	95
Cu-BTC/rGO-A-3	1	15	95

2.3. Measurements

A NanotracWave II Particle Size Zeta Potential Analyzer was used to conduct dynamic light scattering (DLS) studies at 25 °C. A NanoDrop 2000 UV–Vis spectrophotometer was used to perform ultraviolet-visible (UV–Vis) analyses. Moreover, a PerkinElmer Lambda 25 UV–Vis spectrometer was used to measure the percentage of light absorbance. The absorbance percentage in the UV–Vis region was calculated by measuring the reflectance and transmittance of each sample and then using the A=1-T-R equation [21]. For atomic force microscopy (AFM) tests, a Dualscope DS 95–200 DME microscope was used with samples placed on freshly cleaved mica substrates. The microscope was equipped with a rectangular

aluminum-coated cantilever, and tests were performed at a scan rate of 5 μm/s in the non-contact mode.

X-ray diffraction (XRD) patterns were obtained using a Philips PW1730 X-Ray Diffractometer equipped with a Cu kα radiation source (λ = 1.54056 Å) and tests were performed at 40 kV and 30 mA. The Fourier-transform infrared (FTIR) spectroscopy (FTIR) was conducted using a Thermo Nicolet Avatar 360, and field emission scanning electron microscopy (FESEM) tests were done using a TESCAN Mira 3 (15 kV).

The nitrogen adsorption/desorption analyses were conducted using a Belsorp mini II analyzer. The isotherms were taken at 77 K, and the results were analyzed using the BET, BJH, and t-plot theories. Raman spectra were acquired using a Teksan TakRam N1-541 spectrometer at 532 nm. Mechanical compression tests were carried out on a Shimadzu AGS-X testing machine with a speed of 1 mm/min and three repeats for each sample.

The evaporation rate studies were performed using a setup described in the literature [6]. A multi-light sun simulator with halogen (100 W) and xenon (60 W) light sources (AM 1.5G), a laboratory balance (A&D HR-200), an Infrared thermometer (UNI-T UT303A), and a thermal imaging camera (SATIR Hotfind) was used for the evaporation rate measurement setup. A BloorSpec power meter and a standard silicon solar cell were used to confirm the power density.

Anti-biofouling properties were studied by evaluating the adhesion ability of *Nitzschia* algae [22]. For each assay, 2 mg of the aerogel sample was added to 10 mL of *Nitzschia* suspension, and then the algae were cultured at 25 °C for 12 h light/dark cycles (three repeats for each sample). After each 12 h light culturing cycle, the culture media was stirred and then placed under fluorescent illumination for the next 12 h dark cycle [22]. After each 24 h time interval, the concentration of *Nitzschia* was measured by counting on a hemocytometer via fluorescence

microscope, and the anti-adhesion properties were studied by observing the attachment of *Nitzschia* to the surface [22].

To measure the antibacterial properties of the aerogels, the micro-well diffusion method against Gram-negative *Escherichia coli* (*E. coli* - ATCC 10536) and Gram-positive *Staphylococcus aureus* (*S. aureus* - ATCC 29737) bacteria was used. The bacteria were grown in a 100 ml flask with 10 ml of tryptic soy broth (TSB, Merck) on a rotary shaker (200 rpm) at 37 °C for 5 h. The bacterial suspensions were then diluted to 10^4-10^5 CFU/ml and 100 ml of each diluted bacterial suspension was placed in micro-wells (6 mm in diameter) at concentrations of 3 mg/ml, 2 mg/ml, 1 mg/ml, 0.5 mg/ml, 0.25 mg/ml, 0.125 mg/ml, 62.5 μg/ml, and 3.125 μg/ml.

The minimum inhibitory concentration (MIC) of the samples was determined by incubating the plates at 37°C for 24 hours and observing for samples with no visible bacterial growth. The minimum bactericide concentration (MBC) was determined by observing the lowest concentration of samples yielding colony counts less than 0.1% compared to the initial inoculum. The growth inhibition zone of the samples was also studied by spreading 100 μL of the bacterial suspension over an agar Luria Bertani plate and adding 300 μg and 600 μg (in DMSO) of the samples to wells on the plate. The diameters of the inhibition zones were then measured after incubating the plates at 37°C for 24 hours, and standard deviation values were calculated.

3. Results and discussion

3.1. Characterization of the GO nanosheets

The thickness, exfoliation state, and chemical structure of GO nanosheets used as the precursor for the fabrication of nanocomposite aerogels were characterized using AFM (Figure 2 a and

b), XRD (Figure 2 c), and FTIR (Figure 2 d) methods, respectively. Based on AFM results (Figure 2 a), synthesized GO nanosheets were of single-layer form with a thickness of ~1.5 nm (Figure 2 b). Moreover, the complete oxidation of GO nanosheets was confirmed by the presence of the GO characteristic peak at 2θ values around 10° (Figure 2 c). The oxidation of graphite into GO nanosheets and the presence of oxygen-containing functional groups on the basal plane and edges of nanosheets increase the interlayer spacing in the structure from 0.33 nm for graphite to around 0.88 nm for GO [23].

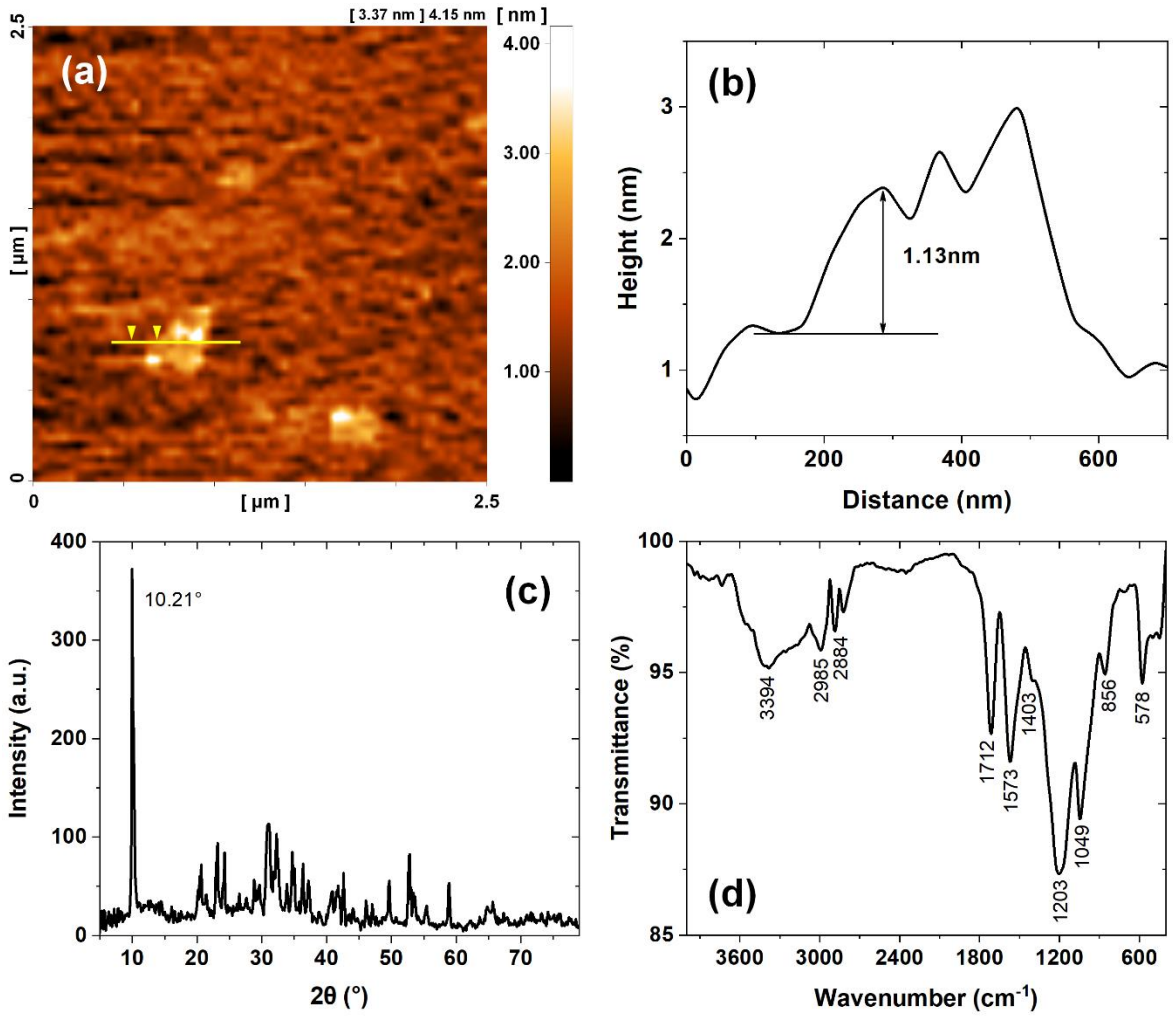

Figure 2. *AFM topographic image (a), height distribution profile (b), XRD pattern (c), and FTIR spectra (d) of the GO nanosheets*

FTIR results were used to investigate the type of oxygen-containing functional groups on GO nanosheets' basal plane and edges (Figure 2 d). The band observed at 3394 cm^{-1} was assigned to stretching vibrations of –OH groups of hydroxyl, COOH, and the remaining moisture in the structure of GO nanosheets [24]. The bands at 2985 and 2884 cm^{-1} were assigned to the asymmetric and symmetric stretching vibrations of –CH groups on the basal plane and edges of GO, respectively [25]. Furthermore, the band at 1712 cm^{-1} was related to the stretching vibration of –C=O (COOH groups) bonds of GO [26, 27].

The band observed at 1573 cm^{-1} was assigned to the overlapping of in-plane asymmetric stretching vibrations of sp^2-hybridized C=C in the basal plane of GO nanosheets and the stretching vibrations of C=O groups in the structure of ketones and 1,3-benzoquinones on the basal plane and edges of the GO nanosheets [28]. In addition, the shoulder observed at 1403 cm^{-1} and two bands observed at 1203 and 1049 cm^{-1} were assigned to the stretching vibrations of C–O in the γ-region (mostly epoxides), β-region (ketones and peroxides), and α-region (mostly ethers), respectively [17, 28].

3.2. Morphology and microstructure of Cu-BTC/rGO nanocomposite aerogels

The FESEM results were used to study the morphology of Cu-BTC NPs, the rGO aerogel prepared without Cu-BTC NPs in the precursor solution (rGO-A), and nanocomposite aerogels prepared using different concentrations of Cu-BTC NPs in the precursor solution (Cu-BTC/rGO-A-1, Cu-BTC/rGO-A-2, and Cu-BTC/rGO-A-3), as shown in **Figure 3**. The rGO aerogel (Figure 3 a) presented a three-dimensional porous and interconnected structure with a high surface area well-suited for interfacial evaporation. This structure is formed by the folding and crumpling of GO through the reduction process, which results in the formation of a three-

dimensional structure with rGO nanosheets that are connected through the π-π interaction mechanism [29].

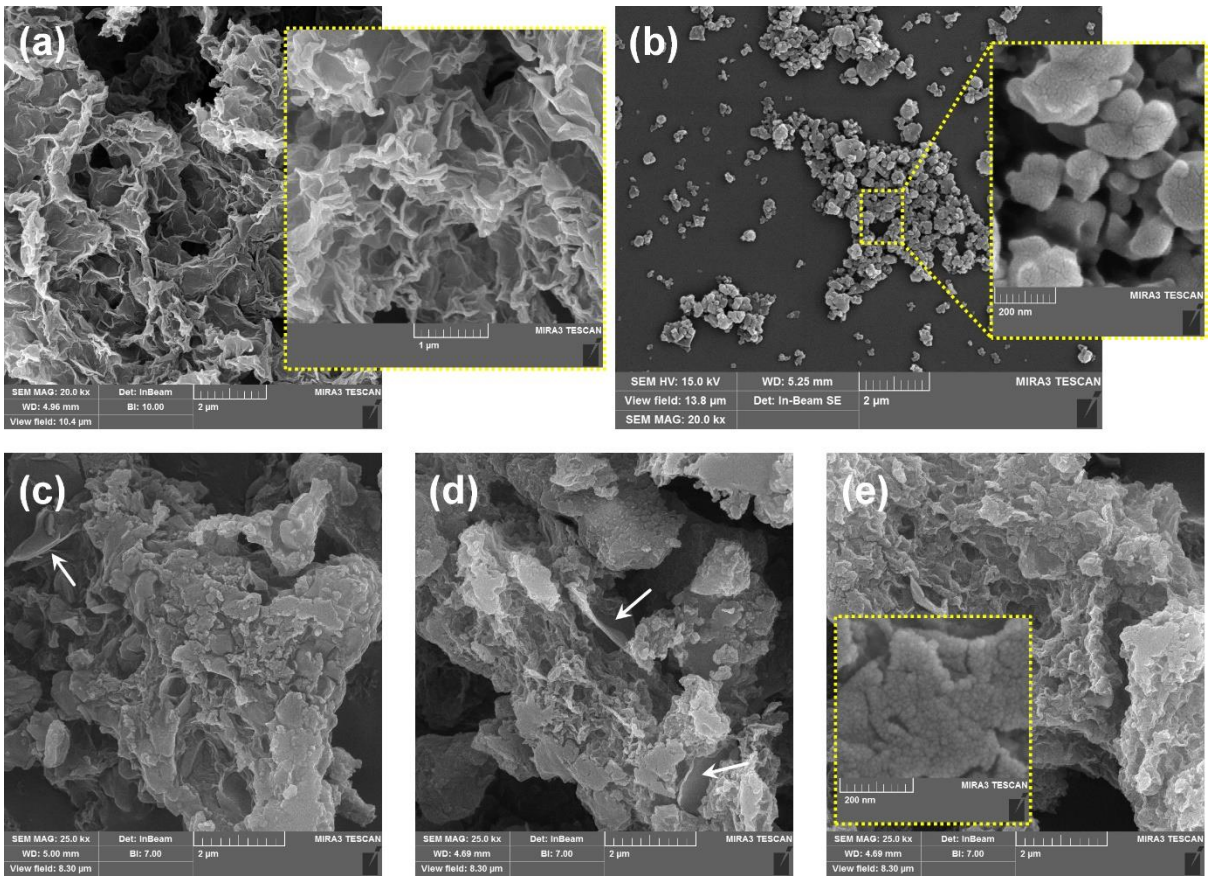

Figure 3. *FESEM images of rGO-A (a), Cu-BTC NPs (b), Cu-BTC/rGO-A-1 (c), Cu-BTC/rGO-A-2 (d), and Cu-BTC/rGO-A-3 (e)*

With the progress of the reduction process of GO into rGO nanosheets, the basal plane of rGO nanosheets becomes more unsaturated and thus has more available sites for π-π interaction between the nanosheets. Moreover, the folding and crumpling of GO nanosheets during the reduction process which is facilitated by the low thickness of the nanosheets (Figure 3 b) lead to easier interconnection between the GO nanosheets, resulting in a three-dimensional structure with a high specific surface area and a large number of active sites for the attachment of Cu-BTC NPs.

Cu-BTC NPs had a semi-spherical shape (Figure 3 b), which is known to be the dominant morphology for Cu-BTC porous structures synthesized through ultrasound irradiation under solid-state conditions [17]. For all of the nanocomposite aerogels (Figure 3 c-e), the Cu-BTC NPs were attached to the surface of rGO nanosheets, forming nanocomposite aerogels. Based on our recent work, Cu-BTC NPs have the potential for physical interactions with molecular imperfection sites, epoxides, and carboxyl groups in the structure of GO [17]. This interaction between GO nanosheets and Cu-BTC NPs in the precursor solutions used to fabricate the nanocomposite aerogels resulted in the surface of the aerogels being decorated with Cu-BTC NPs. The content of Cu-BTC NPs adhered to the surface of the rGO aerogels increased as the content of Cu-BTC NPs in the precursor solutions used for the fabrication of the nanocomposite aerogels increased (Figure 3 c-e).

Since there were regions without adhered Cu-BTC NPs on the basal plane of rGO nanosheets in Figure 3 c and Figure 3 d (indicated with arrows) and the surface of all rGO nanosheets was covered with Cu-BTC NPs in Figure 3 e, it can be concluded that the complete coverage of rGO nanosheets with Cu-BTC NPs was only achieved when the concentration of Cu-BTC NPs in the precursor solution reached a certain optimal content. Beyond this optimal concentration (1 mg/ml in this work), any additional content of Cu-BTC NPs did not enter the structure of nanocomposite aerogels, as the main mechanism for adhesion of Cu-BTC NPs to the surface of the rGO nanosheets was through interfacial interactions.

FTIR spectra of prepared samples were used to indirectly study the mechanism of interactions between rGO and Cu-BTC NPs (**Figure 4)**. Bands observed at 1014, 1180, and 1403 cm^{-1} in the FTIR of the rGO aerogel (Figure 4 a) were related to the stretching vibrations of –C–O bonds on the basal plane and edges of rGO nanosheets in the structure of the rGO aerogel (α-region, β-region, and γ-region, respectively) [28]. Compared to the FTIR results of GO

nanosheets (Figure 2 d), the relative intensity of bands related to –C–O bonds in the α and β regions significantly reduced in the FTIR of the rGO aerogel (Table S1).

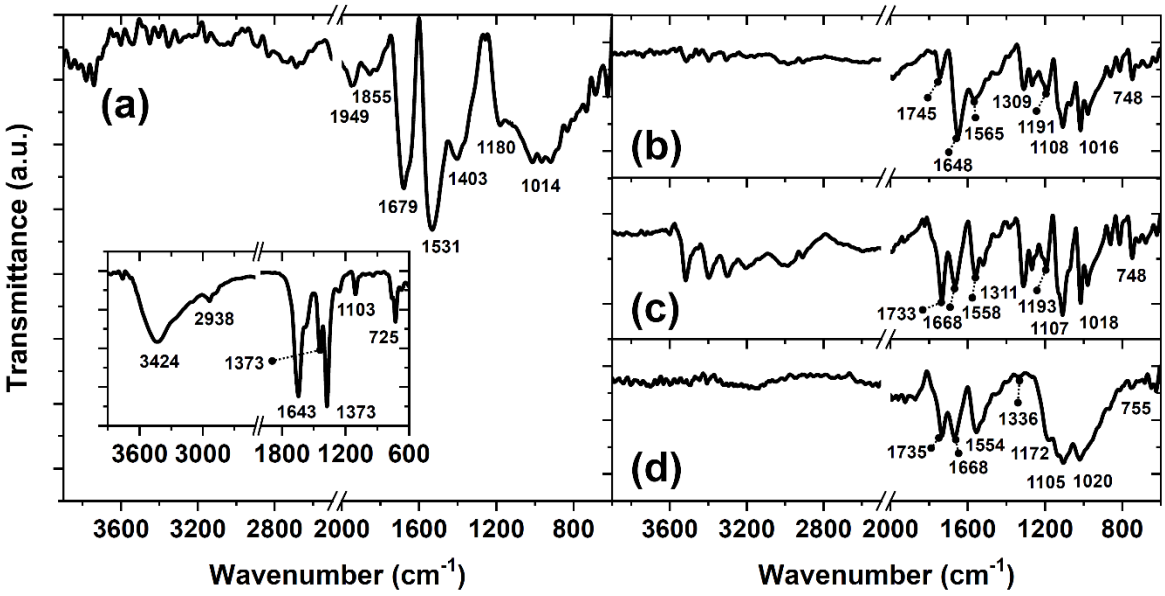

Figure 4. *FTIR spectra of rGO-A (a), Cu-BTC NPs (inset in a), Cu-BTC/rGO-A-1 (b), Cu-BTC/rGO-A-2 (c), and Cu-BTC/rGO-A-3 (d)*

Bands representing the –C–O bonding in the α-region (900-1100 cm^{-1}) were related to ethers (peroxides, furans, dioxolanes) with weaker contributions from hydroxyls and carboxyls, and bands in the β-region (1100-1280 cm^{-1}) were related to ketones (pyrones and γ-butyrolactones) [28]. Moreover, bands in the γ-region (1280-1500 cm^{-1}) were assigned to epoxides on the basal plane and edges of GO/rGO nanosheets [28, 30]. Consequently, the hydrothermal reduction of GO into the three-dimensional rGO most effectively resulted in the elimination of ketones (C=O, –C–O β-region). Moreover, ethers and hydroxyls were also more effectively reduced through the reduction process, compared to epoxides in the structure of aerogels. In addition, considering the high relative intensity of the carboxyls representative bands in the structure of

GO nanosheets and the rGO aerogel (1679 cm^{-1} in Figure 4 a and 1712 cm^{-1} in Figure 2 d), the reduction process did not affect the content of carboxyls (Table S1).

When Cu-BTC NPs were added to the structure of rGO porous nanostructures (Figure 4 b-d), a change in the relative intensities of the bands related to sp^2-hybridized C=C bonding (bands in the range of ∼1500-1600 cm^{-1}) and carboxyls (bands in the range of ∼1600-1750 cm^{-1}) was observed. Since the band assigned to –O–C–O– bonding of BTC parts in the structure of Cu-BTC NPs is expected at around 1643 cm^{-1} (inset in Figure 4 a), the higher relative intensity of the band observed in the range of ∼1600-1750 cm^{-1} in the FTIR spectra of nanocomposite aerogels can be related to the overlapping of the BTC band (in the structure of Cu-BTC NPs) and the carboxyl groups-related band (in the structure of rGO aerogels).

Bands observed in the range of 670–770 cm^{-1} in Figure 4 b-d were related to the Cu-O bonding in the structure of Cu-BTC NPs. Moreover, the band observed at ~1105 cm^{-1} was assigned to the C–O–Cu bonding in the structure of Cu-BTC NPs. Considering the observed reduction in the relative intensity of the band assigned to the Cu-O bonding at ~755 cm^{-1} with an increase in the content of Cu-BTC NPs in nanocomposite aerogels, a possible interaction mechanism between rGO and Cu-BTC NPs is the formation of interfacial interactions between the oxygen-containing functional groups of rGO and the Cu sites of Cu-BTC NPs, as also suggested in the literature [31]. As the characteristic band of epoxy groups almost disappeared in the FTIR spectra of nanocomposite aerogels, the most possible interaction mechanism can be the formation of interactions between Cu sites of Cu-BTC NPs and epoxy groups of rGO. However, considering the three-dimensional structure of Cu-BTC NPs, the formation of π-π interactions between BTC regions in Cu-BTC macromolecules and the sp^2-hybridized C=C bonding in the backbone of rGO is also a possible interaction mechanism, specifically through final steps of the hydrothermal reduction process and with an increase in the content of C=C bonding in the backbone of rGO.

The microstructure of the fabricated nanocomposite aerogels was studied using XRD results **(Figure 5)**. No peak was observed in the XRD pattern of the rGO aerogel (Figure 5 a), indicating the exfoliation of rGO nanosheets in the structure of the rGO aerogel. When Cu-BTC NPs were introduced into the structure of aerogels, a weak peak at ~10° was observed in the XRD patterns of nanocomposite aerogels (Figure 5 b-d). The presence of this peak indicates that some GO nanosheets are stacked during the reduction process of nanocomposite aerogels. The relative intensity of this peak decreased as the content of Cu-BTC NPs in the nanocomposite aerogels increased indicating that fewer nanosheets were stacked as more Cu-BTC NPs decorated the surface of the nanosheets.

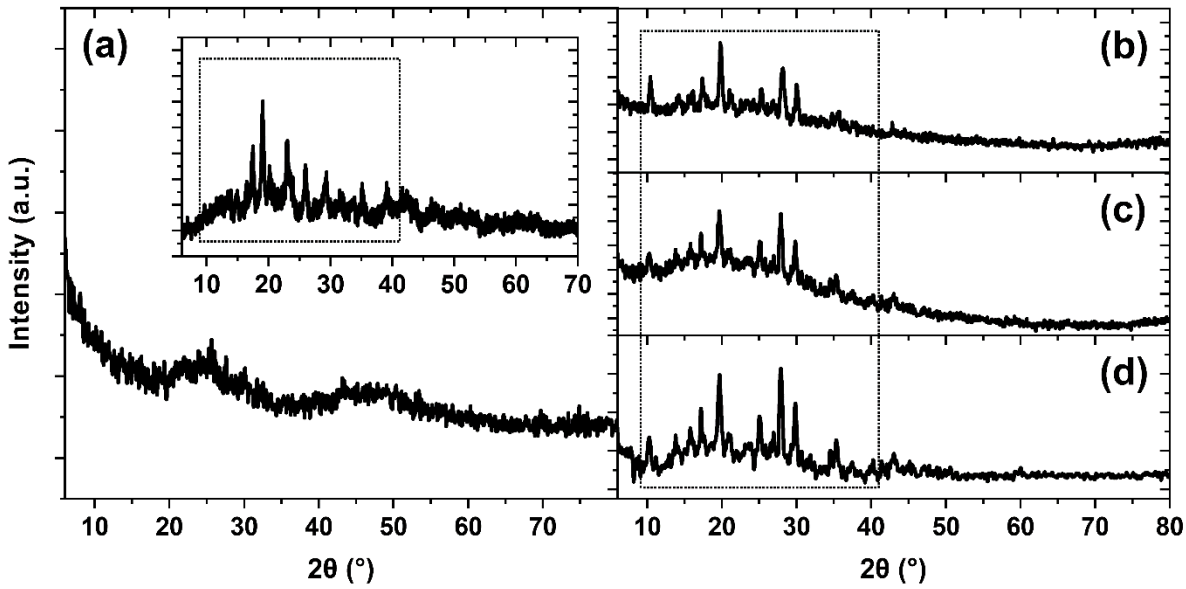

Figure 5. *XRD patterns of rGO-A (a), Cu-BTC NPs (inset in a), Cu-BTC/rGO-A-1 (b), Cu-BTC/rGO-A-2 (c), and Cu-BTC/rGO-A-3 (d)*

Cu-BTC NPs synthesized in this work (inset in Figure 5 a) presented XRD peaks at 2θ values around 13.6° (400), 14.9° (420), 16.3° (422), 17.4° (511), 19.1° (440), 20.2° (442), 22.9° (444), 25.9° (731), 29.3° (751), 35.1° (951), and 39.1° (971), identical to the structure of Cu-BTC

MOFs reported in the literature [17]. No significant change was observed in the microstructure of Cu-BTC NPs in the structure of nanocomposite aerogels (Figure 5 b-d). As Cu-BTC NPs were first synthesized and then added to the structure of nanocomposite aerogels, no change in the microstructural properties of Cu-BTC NPs was expected (Table S2).

Raman spectroscopy results were used to further investigate the impact of the reduction process on the microstructure of nanocomposite aerogels, as shown in **Figure 6**. To analyze the first-order Raman spectra of the aerogels, we used a five-function fitting model with D, G, D', D'', and D* bands, based on the literature [17]. Moreover, we used a four-function fitting model with 2D, 2D', D + D', and G* bands as the main bands for the second-order Raman region. We analyzed the relative intensity ratios and positions of the bands to investigate the structure of rGO in the nanocomposite aerogels. Relative intensity ratios and the position of bands were used to investigate the structure of rGO in nanocomposite aerogels (Table S3).

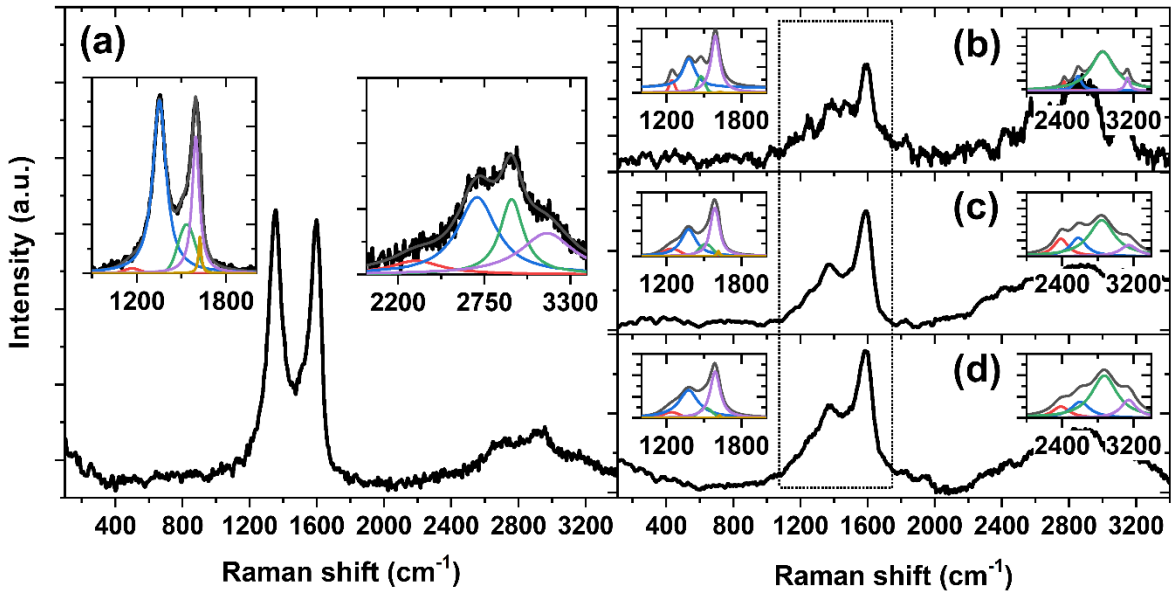

Figure 6. *Raman spectra of rGO-A (a), Cu-BTC/rGO-A-1 (b), Cu-BTC/rGO-A-2 (c), and Cu-BTC/rGO-A-3 (d)*

The G band, expected at ~1585 cm^{-1} for GO and rGO, is related to the first-order E_{2g} optical mode (longitudinal and in-plane transverse) of graphite and is the characteristic band of the sp^2 arrangement in the backbone of graphene-based materials [32]. Moreover, the D band at ~1350 cm^{-1}, becomes Raman active by single-phonon intervalley scattering processes (the A_{1g} breathing mode) and is related to the formation of defects through the oxidation process of GO that alters the basal plane structure of graphene [33]. The intensity ratio of D and G bands (I_D/I_G) can be considered a measure of the oxidation degree of graphene derivatives.

The I_D/I_G ratio of GO nanosheets, which was 1.31 (Figure S2), reduced with the self-assembly of these nanosheets into rGO aerogels to 1.26. This indicates an increase in the concentration of C-sp^2 domains and a reduction in the concentration of C-sp^3 domains. Moreover, the relative intensity of all other defect-related bands reduced with the reduction of GO nanosheets into the rGO aerogel (Table S3), indicating the lower concentration of sp^3 defects in the crystalline structure of rGO nanosheets of the rGO aerogel. The intensity of the G band increased significantly in the structure of nanocomposite aerogels, compared to the rGO aerogel. The I_D/I_G ratios of nanocomposite aerogels were 0.59, 0.55, and 0.60 for Cu-BTC/rGO-A-1, Cu-BTC/rGO-A-2, and Cu-BTC/rGO-A-3, respectively. These values are almost half of the I_D/I_G ratio value of the rGO aerogel (1.26).

The reduction process used for all samples was the same (Figure 4), and the significant reduction in defects-related bands observed in the Raman spectra of nanocomposite aerogels (Figure 6) can be attributed to the interfacial interactions between rGO and Cu-BTC NPs in the structure of nanocomposite aerogels. These interactions likely affected the phonon scattering processes in the Raman scattering analysis. It is noteworthy that based on our recent studies [17], Raman bands of Cu-BTC NPs were not observed in Figure 6, which could be due to the low solid-content concentration of Cu-BTC NPs in the nanocomposite aerogel structure. This

led to overlapping Cu-BTC-related bands with the strong rGO-related bands in the Raman spectra of nanocomposite aerogels.

N_2 adsorption/desorption isotherms were used to study the textural properties of fabricated nanocomposite aerogels, as shown in **Figure 7**. The rGO aerogel presented a type-IV isotherm (Figure 7 a), suggesting the formation of a porous structure mostly consisting of mesopores, as confirmed also in the average pore diameter of the sample in **Table 2**. Moreover, the specific surface area and pore volume of the rGO aerogel prepared in this work (Table 2) were close to the rGO aerogels reported in the literature for the similar concentration of GO in the precursor solution and with AA as the reducing agent [34].

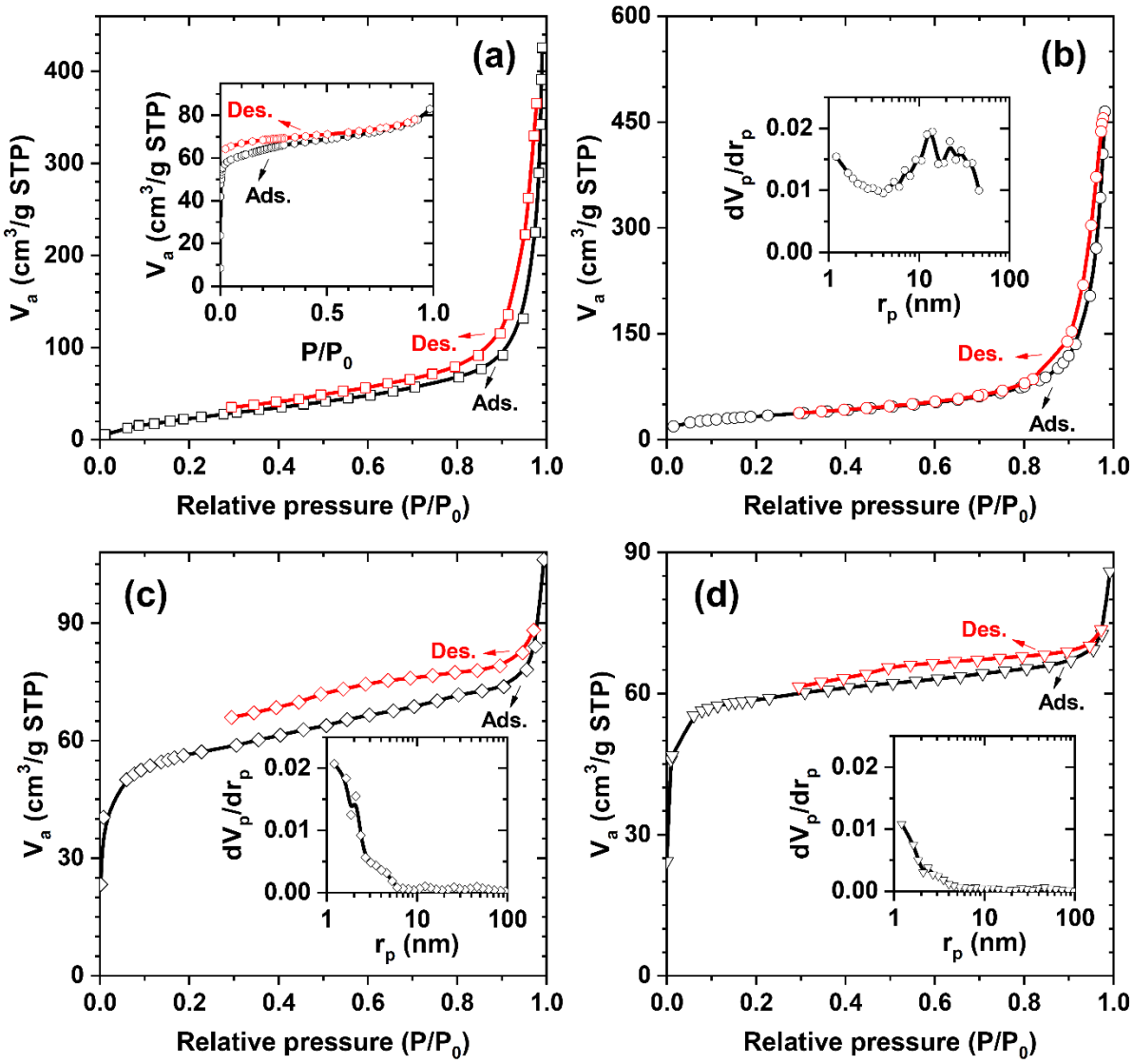

Figure 7. *Nitrogen adsorption/desorption isotherms of rGO-A (a), Cu-BTC NPs (inset in a), Cu-BTC/rGO-A-1 (b), Cu-BTC/rGO-A-2 (c), and Cu-BTC/rGO-A-3 (d)*

Table 2. *Textural properties of samples prepared in this work*

Sample	**BET surface area (m^2/g)**	**Total pore volume (cm^3/g)**	**Average pore diameter (nm)**
rGO-A	103.65	0.65	25.24
Cu-BTC/rGO-A-1	113.81	0.72	26.88
Cu-BTC/rGO-A-2	221.67	0.16	2.94
Cu-BTC/rGO-A-3	232.22	0.13	2.25

When very low contents of Cu-BTC NPs were introduced into the structure of nanocomposite aerogels, the type of ads/des isotherm of the sample did not change (Figure 7 b). However, the specific surface area and the total pore volume of the Cu-BTC/rGO-A-1 sample were slightly higher that the rGO aerogel. As the content of Cu-BTC NPs in the structure of rGO-based nanocomposite aerogels increased, the isotherm of the sample changed into a type-V isotherm, suggesting an increase in the volume of micropores in the texture of the sample (Figure 7 c-d). Moreover, the pore diameter of nanocomposite samples with higher contents of Cu-BTC NPs (Cu-BTC/rGO-A-2 and Cu-BTC/rGO-A-3) reduced to around 2 nm, confirming the formation of microporous structures.

The specific surface area of nanocomposite aerogels showed a linear relationship with the Cu-BTC NPs concentration in the precursor solution. The highest specific surface area of samples prepared in this work was for the nanocomposite aerogel prepared using the highest content of Cu-BTC NPs. Since the specific surface area of Cu-BTC NPs is greater than the rGO aerogel

(~ 244 m^2/g [17], see inset in Figure 7 a for the adsorption isotherm of Cu-BTC NPs), the observed increase in the specific surface area and the isotherm type of nanocomposite aerogels can be related to the presence of Cu-BTC NPs in the structure of samples.

Morphological and structural studies of nanocomposite aerogels showed that the effect of incorporating Cu-BTC NPs was significant when the precursor solution for the hydrothermal self-assembly process contained Cu-BTC NPs at concentrations of 5 mg/ml or higher. In samples prepared using Cu-BTC NPs concentrations ≥ 5 mg/ml, micropores dominated the texture, and a high concentration of C-sp^3 domains was observed in the structure. Furthermore, Cu-BTC NPs were uniformly distributed on the surface of rGO nanosheets in the structure of these nanocomposite aerogels.

3.3. Solar evaporation performance of Cu-BTC/rGO nanocomposite aerogels

The solar evaporation performance of nanocomposite aerogels was evaluated by evaporation rate and efficiency calculations, as shown in **Figure 8**. Steam generation efficiency values (η) were calculated using the following equation [6]:

$$\eta = \frac{m h_{LV}}{C_{opt} q_i}$$

where m, h_{LV}, C_{opt}, and q_i are the water evaporation rate, the liquid-to-vapor phase transition enthalpy, the optical concentration, and the solar irradiation (1 kW/m^2 for 1 sun), respectively [6]. The evaporation rate for each sample is measured using the water mass change (excluding the mass change under the dark condition) with time. Moreover, h_{LV} can be calculated using the following equation [35]:

$$h_{LV} = \lambda + C\Delta T$$

where λ, C, and ΔT are the phase transition latent heat, the specific heat capacity of water (4.2 kJ/kg·K), and the water temperature change, respectively [36].

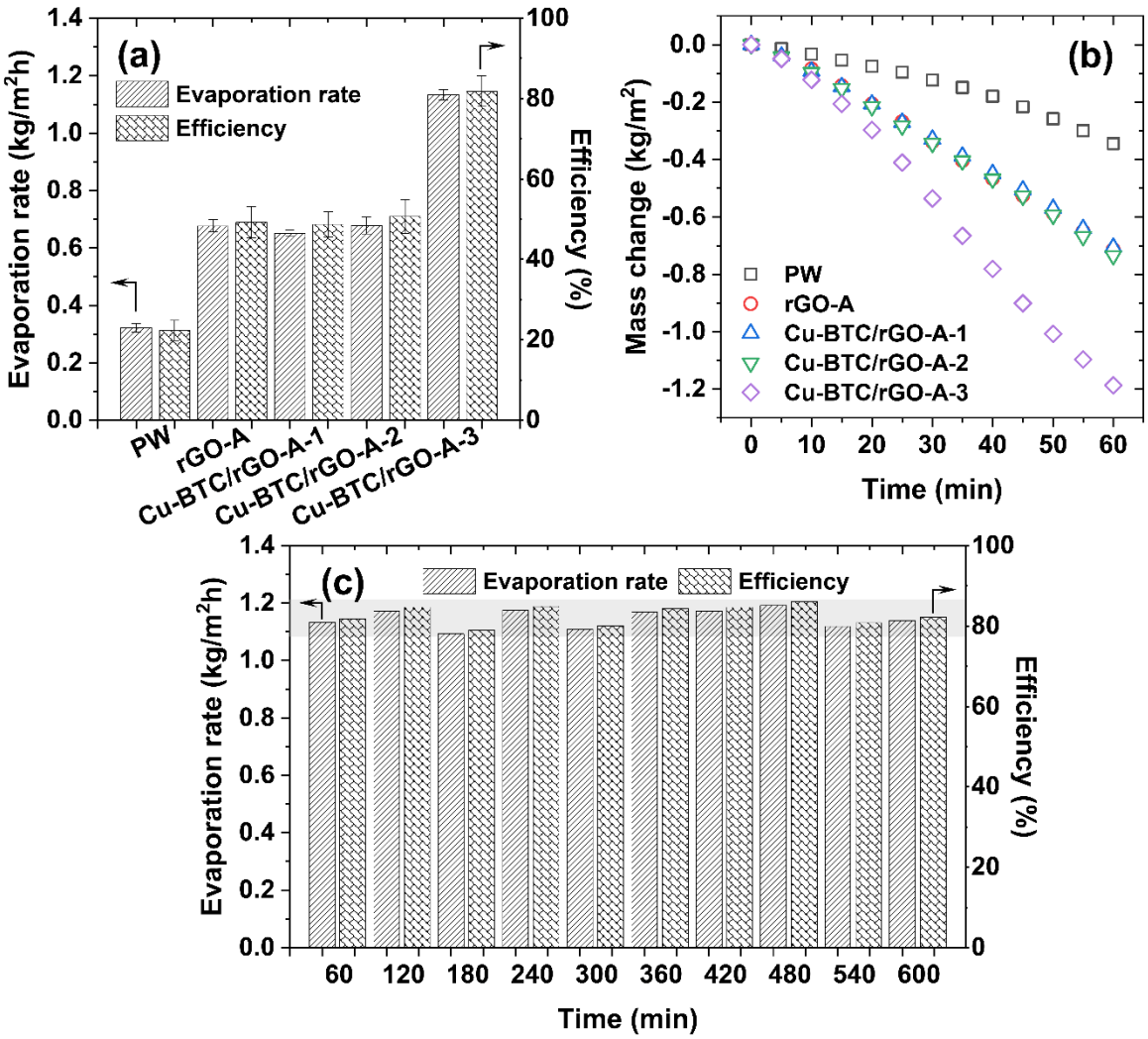

Figure 8. *Solar evaporation rates and efficiencies of fabricated samples (a), mass change of samples with time (b), and the water evaporation performance of the Cu-BTC/rGO-A-3 nanocomposite aerogel through continuous solar illumination for 600 min (c). the highlighted region in panel c represents the highest and lowest evaporation efficiencies (all tests under 1 kW/m^2).*

The evaporation rate of the rGO aerogel was 0.68 kg/m^{2}h, which corresponds to a solar steam generation efficiency of 49.2% (Figure 8 a-b). The evaporation efficiency of the rGO aerogel (49.24%) was more than 26% higher than the solar evaporation efficiency of pure water

(22.34%). When small amounts of Cu-BTC NPs were introduced into the structure of nanocomposite aerogels, no significant change in the solar evaporation efficiency of active materials was observed. The solar evaporation efficiency of the Cu-BTC/rGO-A-2 nanocomposite aerogel was 50.7%, which is 1.5% higher than the solar evaporation efficiency of the rGO aerogel. The limited impact of introducing low contents of Cu-BTC NPs on the solar evaporation efficiency of the system can be related to the BET surface area and the pore size of samples prepared from low contents of Cu-BTC NPs in the hydrothermal precursor solutions.

When the content of Cu-BTC NPs increased to the maximum possible amount (Cu-BTC/rGO-A-3 nanocomposite aerogel), the evaporation efficiency of the material increased significantly to 81.8%, which is more than 32% and 59% higher than the solar water evaporation efficiencies of the rGO aerogel and pure water, respectively. The high specific surface area and low pore diameter of the Cu-BTC/rGO-A-3 nanocomposite aerogel resulted in the high water mass change through the solar evaporation process (Figure 8 b) that led to the high interfacial evaporation efficiency of this sample. Moreover, the continuous solar evaporation studies on the Cu-BTC/rGO-A-3 nanocomposite aerogel for 600 min of illumination confirmed the stable solar steam generation performance of this sample through continuous usage (Figure 8 c).

The solar evaporation mechanisms in the structure of graphene-based porous nanostructures are the solar-to-thermal energy conversion and the heat localization mechanisms. The main factors that control these processes are (i) the specific surface area and the pore size of the active material, (ii) the thermal conductivity of the active material, and (iii) the adsorption efficiency of the active material. The Cu-BTC/rGO-A-3 nanocomposite aerogel had a higher specific surface area than the other samples, resulting in a more available surface area for interfacial evaporation.

Moreover, the lower average pore size of this sample led to the improvement of the capillary effect in the pores of the nanocomposite aerogel which resulted in the faster evaporation of water molecules in the presence of the nanocomposite aerogel.

As a measure of the photo-to-thermal energy conversion efficiency, the surface temperature of the pure water without any active material is compared with the rGO-A and Cu-BTC/rGO-A-3 samples in **Figure 9 a**. Under one sun irradiation, the slope of the temperature-time curve of the sample containing the Cu-BTC/rGO-A-3 nanocomposite aerogel was higher than both PW and the rGO-A sample. This can be related to an enhancement in the photo-to-thermal energy conversion efficiency of the system in the presence of the Cu-BTC/rGO-A-3 nanocomposite aerogel. Moreover, the average temperature of systems with nanocomposite aerogels as the active material increased with the content of Cu-BTC NPs in the structure of nanocomposite aerogels (Figures 9 b-g).

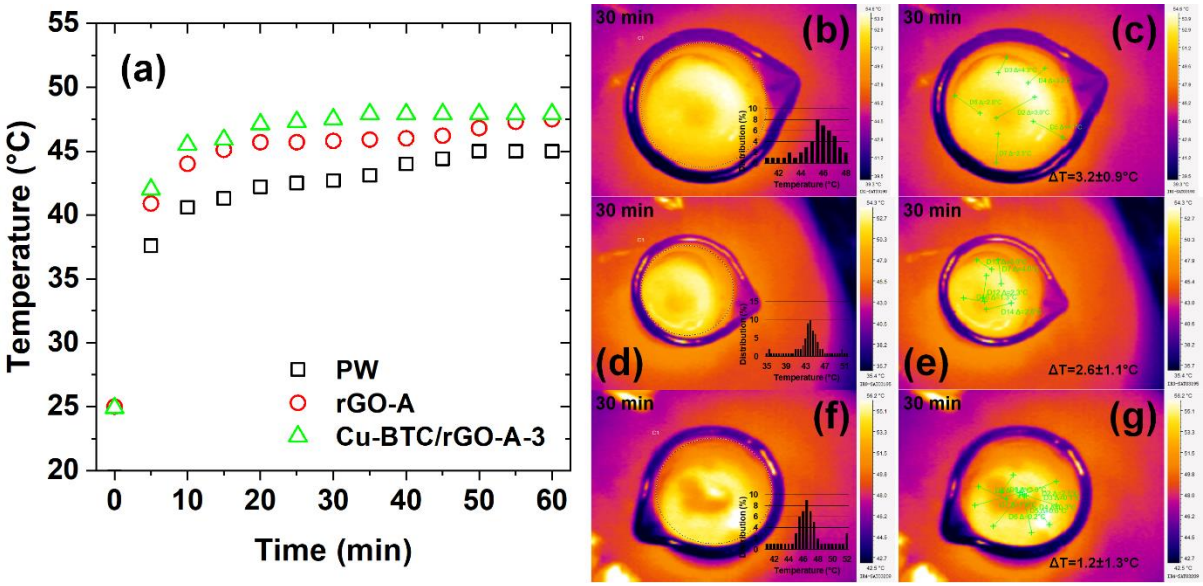

Figure 9. *Temperature-time curves of pure water (PW), rGO-A, and Cu-BTC/rGO-A-3 samples (a), as well as thermal images (left: temperature profiles, right: temperature difference images) of the Cu-BTC/rGO-A-1 (b-c), Cu-BTC/rGO-A-2 (d-e), and Cu-BTC/rGO-A-3 (f-g) samples*

Increasing the content of Cu-BTC NPs in the structure of nanocomposite aerogels did not significantly affect the light absorption of nanocomposite aerogels, as evidenced by the UV-Vis absorption studies (Figure S3). Cu-BTC-based nanostructures have two main absorption peaks in the UV-Vis region, (1) a sharp peak at around 200-250 nm and (2) a wide absorption at around 700 nm [37]. Consequently, these nanostructures can improve the irradiation absorption of nanocomposites mostly in wavelengths below 300 nm. As the high-power solar irradiation is above 300 nm, the incorporation of Cu-BTC NPs in the structure of nanocomposite aerogels only slightly improved the solar absorption performance of Cu-BTC/rGO nanocomposite aerogels (Figure S3) and therefore, this factor cannot be considered as one of the main reasons behind the observed improvement in the solar evaporation performance of nanocomposite aerogels with the content of Cu-BTC NPs in Figures 8 and 9.

The thermal conductivity of the active material is also a factor that affects the solar evaporation process from two perspectives: (i) the heat localization state in the structure of the active material and (ii) the energy dissipation from the active material to the bulk water. The former phenomenon is responsible for interfacial evaporation in the interconnected network of pores in the structure of porous active materials. When light is absorbed, photon-phonon interaction results in the generation of heat in the structure of the active material, and with the localization of the generated heat the temperature of the trapped water in the porous structure of the active material increases, and the phase change from liquid to vapor takes place.

Electron-mediated photon-phonon interaction can be considered the main solar-to-thermal energy harvesting mechanism in graphene-based porous nanostructures. Since optical phonons in graphene-based nanostructures occur at high frequencies, increasing the number of carbon layers can lead to the formation of these phonons at lower frequencies. As there is no direct

path of excitation for phonons at low frequencies, photons are mostly absorbed by high-mobility electrons. Then, the electron-phonon scattering process results in the transfer of gained energy from electrons to phonons.

Oxygen-containing functional groups and other types of defects in the structure of graphene-based nanostructures act as phonon scattering sites and participate in the generation of localized heat by trapping electrons in their defective state and losing energy as heat [21]. This is the main reason behind the lower thermal conductivity of GO, compared to graphene. Under solar irradiation, the electron-mediated photon-phonon interaction in the structure of rGO aerogels results in heat generation and the phonon-scattering caused by oxygen groups (and other molecular defects) remained in the structure of rGO aerogels after the reduction process (Figure 4 and Figure 6) leads to the heat localization. This is a result of the low effective thermal conductivity in the structure of rGO aerogels that not only enhances the interfacial evaporation of water molecules but also reduces the energy dissipation to the bulk water [38].

When Cu-BTC NPs are introduced into the structure of graphene-based porous nanostructures, two main phenomena take place: (i) a reduction in the effective thermal conductivity of the system and (ii) an increase in the water/active material interface. Based on the literature [39], the surface coverage degree of graphene-based nanostructures with metal-organic materials can have a direct impact on the solar evaporation efficiency of these materials. Consequently, the observed increase in the solar evaporation efficiency of fabricated nanocomposite aerogels in this work can be related to two aforementioned phenomena.

Regarding the energy dissipation performance of fabricated nanocomposite aerogels, since the temperature distribution in the system with the Cu-BTC/rGO-A-3 nanocomposite aerogel was narrower than other systems (panels b, d, and f in Figure 9), one can postulate that the energy dissipation in the sample with the Cu-BTC/rGO-A-3 nanocomposite aerogel was less than

other samples in this study. As high heat accumulation on the water/active material interface and low heat losses to bulk water are reported in the literature as elements to reach efficient vapor generation [21], the lower energy dissipation in this sample can be considered the main reason behind its better solar evaporation performance (Figures 8 and 9).

Thermal images of the Cu-BTC/rGO-A-3 nanocomposite aerogel were used to study the influence of irradiation time on the transfer of energy from the aerogel to the surrounding water and, in turn, the solar evaporation of the system as shown in **Figure 10**. As seen in Figure 9, the majority of the temperature increase of the Cu-BTC/rGO-A-3 nanocomposite aerogel under irradiation occurs within the first 10 minutes. The same result was observed in Figure 10, where the maximum temperature of the system (the temperature of the aerogel) increased significantly after 10 min.

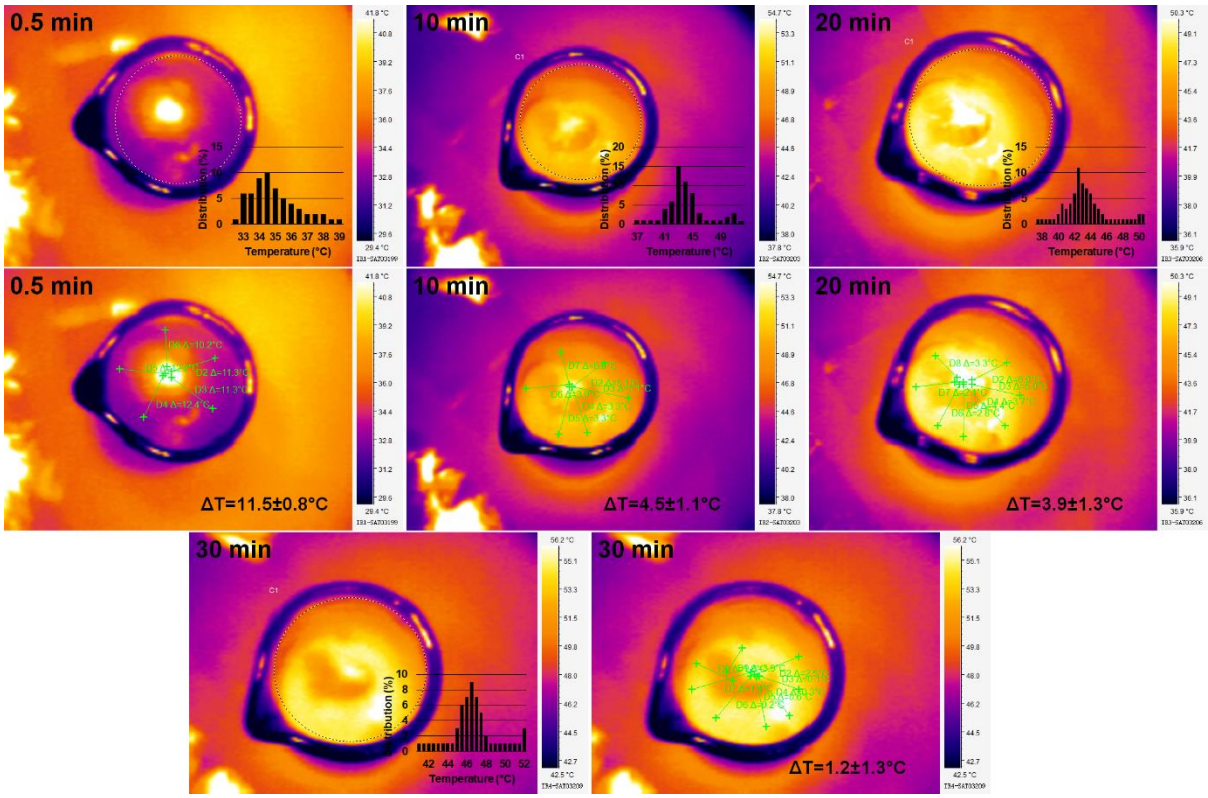

Figure 10. *Thermal images of the Cu-BTC/rGO-A-3 nanocomposite aerogel with the irradiation time under one sun irradiation*

The temperature difference between the aerogel and the bulk water narrows and sharpens over time, as shown in Figure 10. This suggests that the energy dissipation in the system was low initially. As the duration of irradiation increased, the temperature difference decreased and the temperature distribution became wider, indicating an increase in the heat transfer between the active material and the bulk water.

The UV-Vis results of a NaCl solution (5 vol.% NaCl in distilled water) before and after purification using the Cu-BTC/rGO-A-3 nanocomposite aerogel under one sun illumination was used to further analyze the solar evaporation performance of Cu-BTC/rGO nanocomposite aerogels, as shown in **Figure 11**. The UV-Vis of the NaCl solution (Figure 11 a) contained a strong band at around 200 nm and a weak band at around 250 nm, similar to the available reports in the literature [40]. After solar evaporation using the Cu-BTC/rGO-A-3 nanocomposite aerogel as the active material, the intensity of these bands reduced significantly, indicating the successful removal of NaCl and the purification of water.

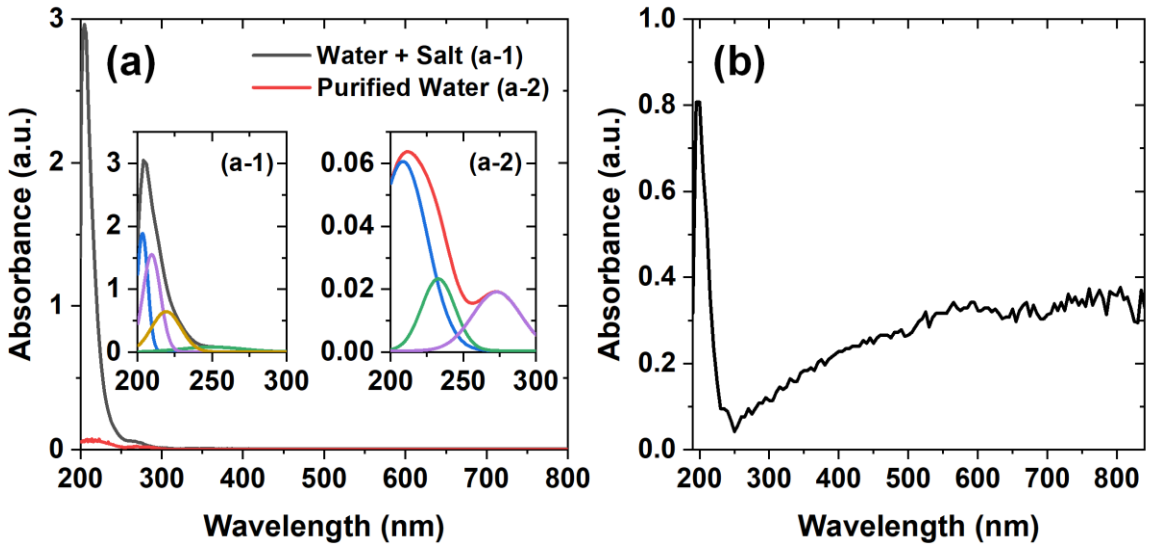

Figure 11. *UV-Vis spectra of the 5 vol.% NaCl solution before and after solar purification with the Cu-BTC/rGO-A-3 nanocomposite aerogel as the active material and under one sun irradiation (a), and the UV-Vis spectra of the Cu-BTC NPs solution in water (b) after sonication (insets in panel a present fitted UV-Vis bands)*

Considering the presence of Cu-BTC NPs in the structure of nanocomposite aerogels, the presence of Cu ions in the purified water was also important. Cu-BTC-based nanostructures have two main absorption peaks in the UV-Vis region (Figure 11 b), (1) a sharp band at around 200-250 nm and (2) a wide absorption at around 700 nm [37]. The absorption peak at around 200 nm is attributed to a ligand-to-metal charge-transfer transition from oxygens to copper ions and the absorption band at around 700 nm is related to the d−d transition of octahedral Cu^{2+} ions [37]. Since no peak was observed at wavelengths above 400 nm in the UV-Vis of the purified water (Figure 11 a), no ions were in the water purified through the solar evaporation of the NaCl solution using the Cu-BTC/rGO-A-3 nanocomposite aerogel as the active material.

3.4. Recyclability and mechanical properties of Cu-BTC/rGO nanocomposite aerogels

The recyclability of the Cu-BTC/rGO-A-3 nanocomposite aerogel for repeated cycles of solar evaporation was evaluated through 10 cycles of irradiation/drying with 0.5 h of irradiation at 1 kW/m^2 in each cycle followed by drying of the sample for the next cycle [6], as shown in **Figure 12**. The Cu-BTC/rGO-A-3 nanocomposite aerogel presented a stable solar evaporation performance through 10 cycles of solar illumination with a mean solar evaporation efficiency of 80.72±2.72%. This indicates the high structural stability of the Cu-BTC/rGO-A-3 nanocomposite aerogel that can be related to two main factors: (1) the mechanical stability of the nanocomposite aerogel through repeated cycles of solar evaporation and (2) the structural

stability of Cu-BTC NPs in the structure of nanocomposite aerogels with repeated cycles of application.

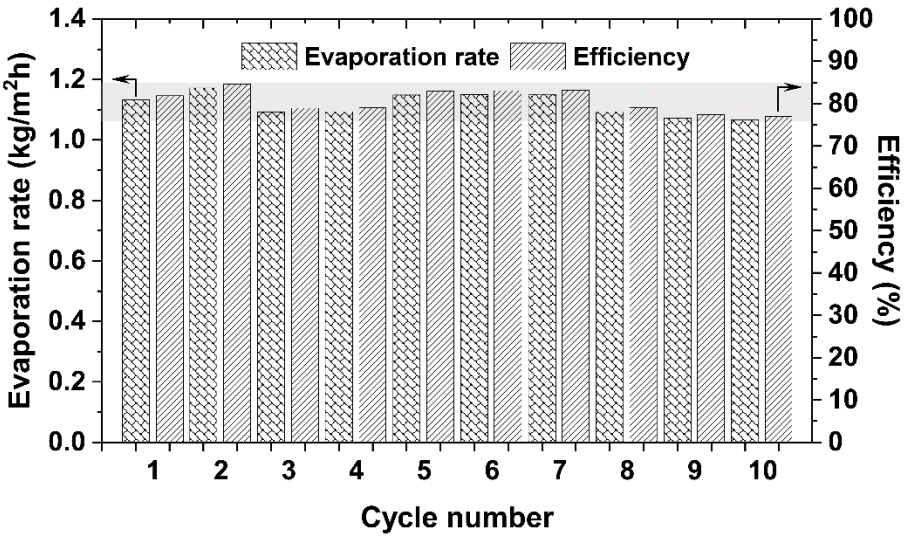

Figure 12. *Recyclability of the Cu-BTC/rGO-A-3 nanocomposite aerogel through 10 cycles of solar illumination (0.5 h of irradiation at 1 kW/m^2 in each cycle, the highlighted region shows the efficiency range of 75–85%)*

The effect of Cu-BTC NPs content on the mechanical properties of Cu-BTC/rGO nanocomposite aerogels was investigated using compressive stress-strain results, as illustrated in Figure 13. As shown by the shift in the compressive stress-strain curves (Figure 13a), the Cu-BTC/rGO nanocomposite aerogel structure became more elastic with the increasing loading content of Cu-BTC NPs. Since Cu-BTC NPs are inherently elastic, their introduction increased the elastic modulus (Figure 13b and c) while reducing the maximum strength of the nanocomposite aerogels (Figure 13d).

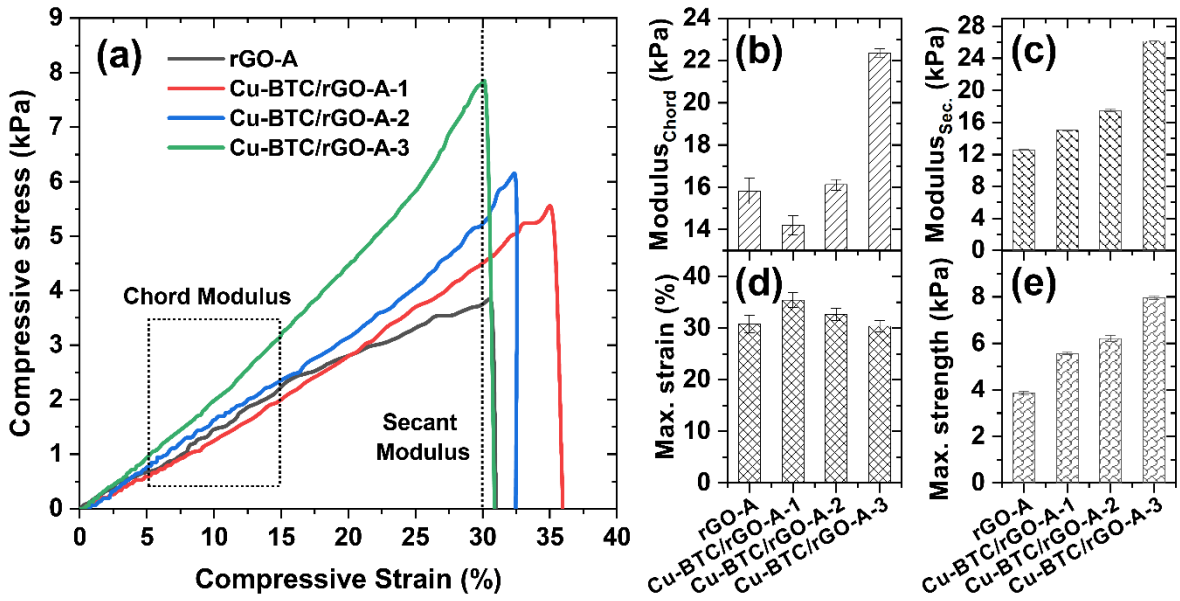

Figure 13. *Compressive stress-strain curves (a), chord modulus between 5% and 15% strains (b), secant modulus at 30% strain (c), maximum strain (d), and maximum strength (e) of fabricated samples*

Cu-BTC NPs are well-known elastic nanomaterials that can withstand more than 2 GPa of compression loading [41]. However, these nanoparticles are very rigid and cannot exhibit any viscoelastic behavior, and this is the reason for the great research interest in introducing Cu-BTC NPs and other metal-organic nanomaterials into the structure of nanocomposites [41]. Moreover, rGO aerogels are porous materials that can provide a good degree of flexibility, as evidenced by the maximum strain of ~30% for the rGO-A sample in Figure 13.

Interestingly, when a low concentration of Cu-BTC NPs was introduced into the structure of Cu-BTC/rGO nanocomposite aerogels (Cu-BTC/rGO-A-1), elastic modulus and maximum strain both increased significantly. This implies that the introduction of a small number of Cu-BTC NPs enhances the flexibility of nanocomposite aerogels while maintaining their mechanical strength. This can be attributed to the improved interfacial interactions between

Cu-BTC NPs and rGO aerogels at low concentrations, leading to the formation of a more homogeneous and flexible nanocomposite structure.

Since a shift in the slope of the stress-strain curves of the rGO-A sample and the Cu-BTC/rGO-A-1 nanocomposite aerogel was observed in Figure 13 a, we extracted two chord modulus and secant modulus values to have a better understanding of the impact of Cu-BTC NPs on mechanical properties of fabricated samples (Figure 13 b and c) [42]. In both cases, the elastic modulus of Cu-BTC/rGO nanocomposite aerogels increased with the loading content of Cu-BTC NPs.

When the loading content of Cu-BTC NPs increased (Cu-BTC/rGO-A-2 and Cu-BTC/rGO-A-3), the rigid behavior of Cu-BTC NPs became more dominant in Cu-BTC/rGO nanocomposite aerogels and the elastic moduli and maximum strains increased and decreased, respectively. The Cu-BTC/rGO-A-3 sample which contained the highest amount of Cu-BTC NPs presented a maximum strain of 30.37 % (Figure 13 d) which was almost equal to the maximum strain of the rGO-A sample. Moreover, the maximum strength of Cu-BTC/rGO-A-3 was 7.96 kPa, which was 106% higher than that of the rGO-A sample. Consequently, the observed recyclability of the Cu-BTC/rGO-A-3 sample in Figure 12 was related to the structural stability of this nanocomposite aerogel.

3.5. Antibacterial and anti-biofouling properties of Cu-BTC/rGO nanocomposite aerogels

Biofouling by microorganisms can lead to the closure of pores and the water uptake channels in the structure of solar active materials [19]. This is an important factor that can affect the long-term purification performance of solar evaporation systems in a complex marine environment [35]. Anti-biofouling properties of Cu-BTC/rGO nanocomposite aerogels were studied using *Nitzschia* as the microorganism, as shown in **Figure 14**. This microorganism is

a typical diatom in the marine environment that can easily adhere to surfaces [43] and hence, its adherence to the surface of Cu-BTC/rGO nanocomposite aerogels (Figure S4) can alter the long-term performance of nanocomposite aerogels in the wastewater purification application.

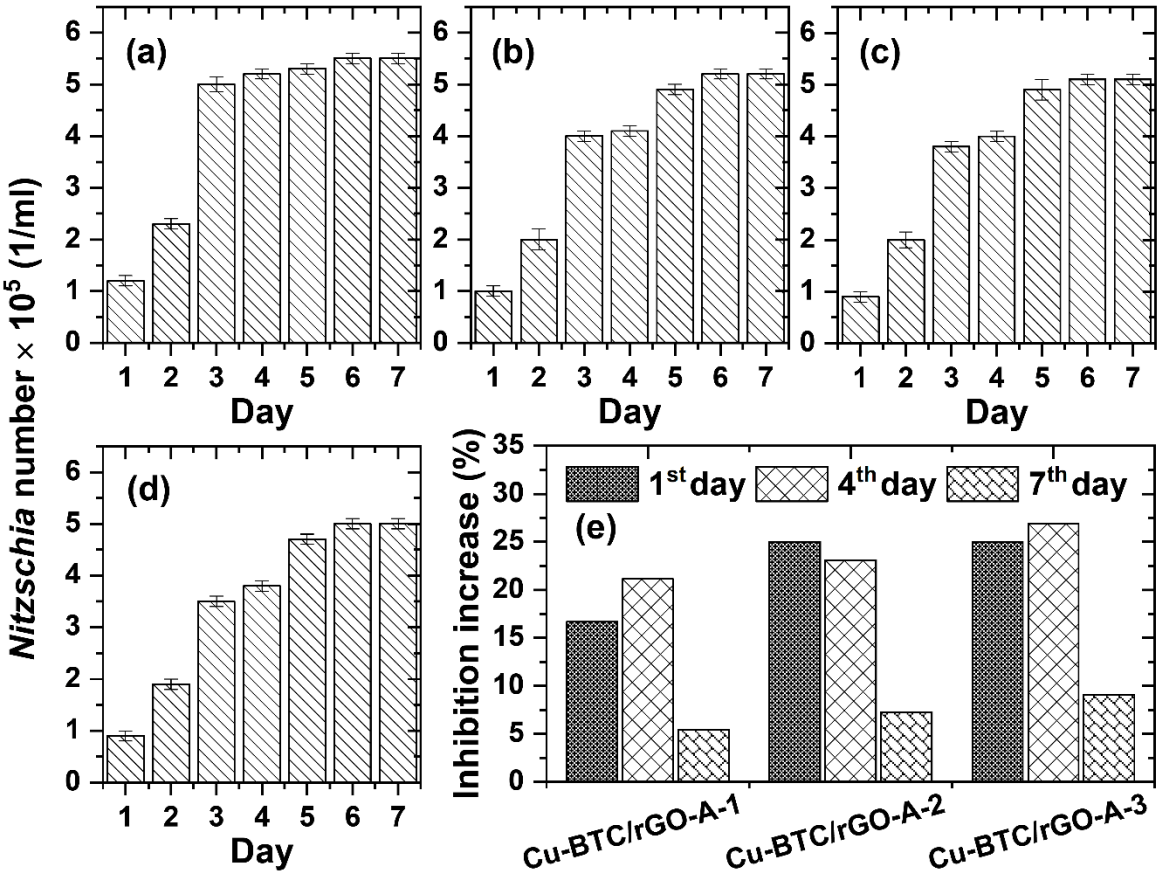

Figure 14. *Nitzschia density in the culture media containing rGO-A (a), Cu-BTC/rGO-A-1 (b), Cu-BTC/rGO-A-2 (c), and Cu-BTC/rGO-A-3 (d) at different culturing time intervals, and a comparison between the microorganism growth inhibition performance of Cu-BTC/rGO nanocomposite aerogels and the rGO-A sample at different days of incubation (e)*

The content of loaded Cu-BTC NPs in the structure of Cu-BTC/rGO nanocomposite aerogels had an indirect relation with the density of *Nitzschia* all over the 7 days of incubation (Figure 14 a-d). To have a better measure of such behavior, the percentage decrease in the density of

Nitzschia at 1st, 4th, and 7th days of incubation for culture media containing Cu-BTC/rGO nanocomposite aerogels compared to the one containing the rGO-A sample was presented in Figure 14 e. Compared to the rGO-A sample, the Cu-BTC/rGO-A-1 sample presented 16, 21, and 5% of *Nitzschia* density reduction at the 1st, 4th, and 7th days of incubation, respectively. Moreover, 25, 27, and 9% of *Nitzschia* density reduction was achieved for the Cu-BTC/rGO-A-3 sample, compared to the rGO-A. Therefore, the microorganism growth inhibition increased with the content of Cu-BTC NPs in the structure of Cu-BTC/rGO nanocomposite aerogels.

The antibacterial properties of the Cu-BTC/rGO-A-3 nanocomposite aerogel, which had the highest solar evaporation performance, were studied using the diameter of the inhabitation zone, minimum inhibitory concentration (MIC), and minimum bactericide concentration (MBC) assays. As shown in **Figure 15**, the growth of *E. coli* was inhibited when the content of the Cu-BTC/rGO-A-3 aerogel in the micro-well was 600 μg, whereas no significant inhibition was observed at a concentration of 300 μg. In contrast, both concentrations of 300 and 600 μg of the Cu-BTC/rGO-A-3 nanocomposite aerogel effectively inhibited the growth of *S. aureus*.

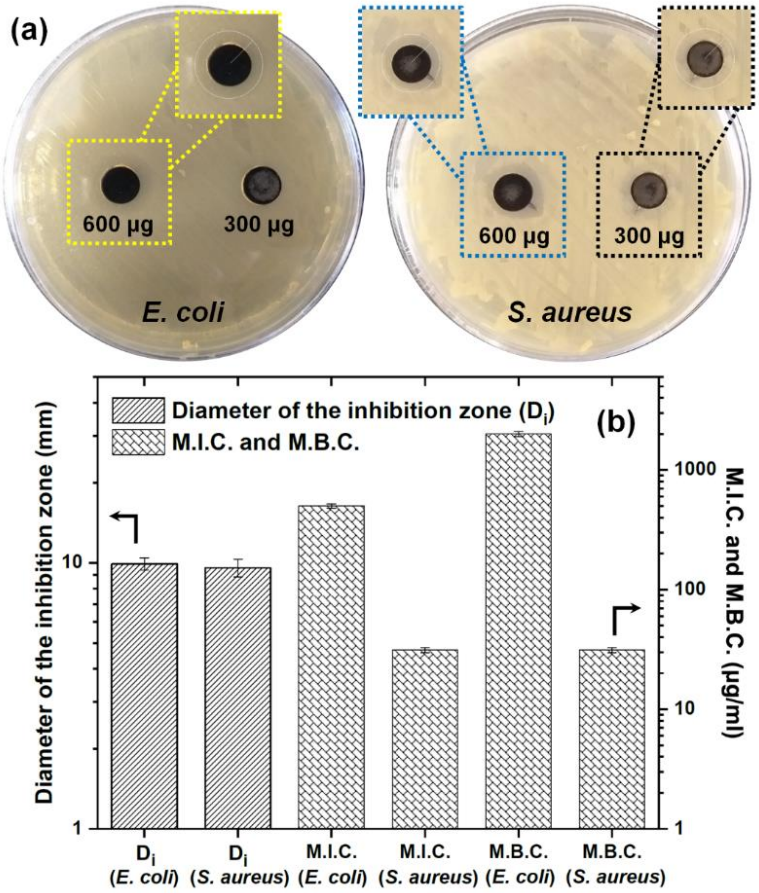

Figure 15. *Images of the bacterial growth inhabitation zones at two concentrations of 300 and 600 µg (a) and the diameter of the inhibition zone, MIC, and MBC results (b) of the Cu-BTC/rGO-A-3 nanocomposite aerogel against S. aureus and E. coli*

Based on our previous studies, the antibacterial activity of Cu-BTC NPs is higher against *S. aureus* than against *E. coli* [17], which is attributed to the presence of a bacterial outer membrane in *E. coli* that improves the resistance of this bacterial strain against toxicity mechanisms [17]. As shown in Figure 15, the Cu-BTC/rGO-A-3 nanocomposite aerogel displayed similar behavior, suggesting that its antibacterial activity is influenced by two parallel mechanisms: (i) the antibacterial activity of the attached Cu-BTC NPs through the formation of Cu ions (Cu^{2+} and Cu^{+}) [17] and (ii) the antibacterial activity of the rGO aerogel via trapping mechanism [44]. The same behavior was observed for the MIC and MBC of the

nanocomposite aerogel with both MIC and MBC values of *E. coli* greater than *S. aureus*, confirming that the presence of the bacterial outer membrane in Gram-negative bacteria limited the effects of the reaction oxide species (ROS) generation on the bacterial membrane [17].

We have discussed the proposed antibacterial activity mechanism of Cu-BTC NPs in our recent publication [17]. When Cu-BTC NPs are introduced into rGO aerogels, the release rate of copper ions increases, resulting in appropriate antibacterial activity of the Cu-BTC/rGO-A-3 nanocomposite aerogel. Despite having a lower specific surface area than Cu-BTC NPs, this nanocomposite aerogel still exhibited proper antibacterial activity. Therefore, the solar evaporation process affected by bacteria not only leads to solar purification but also the removal of bacteria and algae from the final purified water.

Compared to other graphene-based nanocomposite aerogels for antibacterial evaporation, the method followed in this work for the fabrication of a stable and efficient antibacterial evaporator was fast and straightforward. Nanocomposite rGO-based solar evaporator aerogels decorated with polymers like polypyrrole [14] or metal nanostructures such as Ag-MnO_2 [12] or Mxene [45] can present antibacterial activity and solar evaporation efficiencies around 90%. However, in this work, we used a very common class of metal-organic nanostructure to fabricate a new class of rGO aerogel-based solar evaporators with antibacterial and anti-biofouling properties and good stability for the continuous solar evaporation of contaminated wastewater.

4. Conclusions

This study demonstrates that Cu-BTC/rGO nanocomposite aerogels have great potential for various applications in areas such as energy harvesting, energy conversion, and biomaterials. The incorporation of Cu-BTC NPs impacted the morphology and structure of nanocomposite

aerogels, particularly when the concentration of Cu-BTC NPs in the precursor solution was greater or equal to 1 mg/ml. In these samples, micropores dominated the texture, and a high concentration of C-sp^3 domains was observed in the structure. The Cu-BTC/rGO-A-3 nanocomposite aerogel exhibited the highest solar evaporation efficiency of 81.8%. This high efficiency can be attributed to the aerogel's high specific surface area and low pore diameter which provided a large surface for interfacial evaporation. The electron-mediated photon-phonon interaction in the structure of the nanocomposite aerogel also led to heat localization and reduced energy dissipation to bulk water. Furthermore, the Cu-BTC/rGO-A-3 nanocomposite aerogel showed antibacterial activity against both *S. aureus* and *E. coli*. This indicates that the Cu-BTC/rGO-A-3 nanocomposite aerogel not only provides efficient solar water evaporation but can also be used for the general solar purification of water from bacterial contaminants. Future research should focus on optimizing synthesis conditions and post-synthesis treatments to produce more efficient nanocomposite aerogels with enhanced properties.

Acknowledgments

This project has received funding from the European Union's Horizon 2020 research and innovation programme under grant agreement No 101034324. Moreover, A. A. and A. S. would like to acknowledge the financial support provided by the ULB programme: actions blanches.

References

[1] M.S. Irshad, Y. Hao, N. Arshad, M. Alomar, L. Lin, X. Li, S. Wageh, O.A. Al-Hartomy, A.G. Al-Sehemi, V.-D. Dao, H. Wang, X. Wang, H. Zhang, Highly charged solar evaporator toward sustainable energy transition for in-situ freshwater & power generation, Chemical Engineering Journal 458 (2023) 141431. https://doi.org/10.1016/j.cej.2023.141431.

[2] B.R. Scanlon, S. Fakhreddine, A. Rateb, I. de Graaf, J. Famiglietti, T. Gleeson, R.Q. Grafton, E. Jobbagy, S. Kebede, S.R. Kolusu, L.F. Konikow, D. Long, M. Mekonnen, H.M. Schmied, A. Mukherjee, A. MacDonald, R.C. Reedy, M. Shamsudduha, C.T. Simmons, A. Sun, R.G. Taylor, K.G. Villholth, C.J. Vörösmarty, C. Zheng, Global water resources and the role of groundwater in a resilient water future, Nature Reviews Earth & Environment 4(2) (2023) 87-101. https://doi.org/10.1038/s43017-022-00378-6.

[3] R. Sharma, P. Malaviya, Ecosystem services and climate action from a circular bioeconomy perspective, Renewable and Sustainable Energy Reviews 175 (2023) 113164. https://doi.org/10.1016/j.rser.2023.113164.

[4] R. Niu, Y. Ding, L. Hao, J. Ren, J. Gong, J. Qu, Plant-Mimetic Vertical-Channel Hydrogels for Synergistic Water Purification and Interfacial Water Evaporation, ACS Applied Materials & Interfaces 14(40) (2022) 45533-45544. https://doi.org/10.1021/acsami.2c14773.

[5] S. Li, D. Liu, Y. He, M. Li, X. Yang, Y. He, L. Zhou, H. Xie, H. Liu, Multifunction Hybrid Aerogel Capable of Reducing Silver Ions during Solar-Driven Interfacial Evaporation, ACS Sustainable Chemistry & Engineering 10(23) (2022) 7463-7472. https://doi.org/10.1021/acssuschemeng.1c08702.

[6] A. Allahbakhsh, Nitrogen-doped graphene quantum dots hydrogels for highly efficient solar steam generation, Desalination 517 (2021) 115264. https://doi.org/10.1016/j.desal.2021.115264.

[7] M.S. Irshad, N. Arshad, X. Wang, Nanoenabled Photothermal Materials for Clean Water Production, Global Challenges 5(1) (2020) 2000055. https://doi.org/10.1002/gch2.202000055.

[8] C. Wang, Y. Wang, M. Yan, W. Zhang, P. Wang, W. Guan, S. Zhang, L. Yu, J. Feng, Z. Gan, Highly efficient self-floating jellyfish-like solar steam generators based on the partially carbonized Enteromorpha aerogel, J. Colloid Interface Sci. 630 (2023) 297-305. https://doi.org/https://doi.org/10.1016/j.jcis.2022.09.133.

[9] T. Cui, W. Cai, F. Chu, Z. Li, Y. Zheng, Z. Gui, Y. Hu, Enhanced light trapping effect of hierarchical structure assembled from flower-like cobalt tetroxide and 3D-printed structure for efficient solar evaporation, Chem. Eng. J. 451 (2023) 139102. https://doi.org/10.1016/j.cej.2022.139102.

[10] L. Zhao, Z. Yang, J. Wang, Y. Zhou, P. Cao, J. Zhang, P. Yuan, Y. Zhang, Q. Li, Boosting solar-powered interfacial water evaporation by architecting 3D interconnected polymetric network in CNT cellular structure, Chem. Eng. J. 451 (2023) 138676. https://doi.org/10.1016/j.cej.2022.138676.

[11] S. Wu, S. Tian, R. Jian, L. Zhou, T. Luo, G. Xiong, Bio-inspired salt-fouling resistant graphene evaporators for solar desalination of hypersaline brines, Desalination 546 (2023) 116197. https://doi.org/10.1016/j.desal.2022.116197.

[12] Y. Tian, C. Du, S. Yong, X. Zhou, C. Zhou, S. Yang, Catalysis-involved 3D N-doped graphene aerogel achieves a superior solar water purification rate and efficiency, Chem. Eng. J. 453 (2023) 139793. https://doi.org/10.1016/j.cej.2022.139793.

[13] N. Li, J. Wu, R. Su, N. Zhang, J. Zhao, Z. Wang, Bioinspired green tea waste/graphene aerogel for solar-enhanced uranium extraction from seawater, Desalination 545 (2023) 116153. https://doi.org/10.1016/j.desal.2022.116153.

[14] M. Zhang, F. Xu, W. Liu, Y. Hou, L. Su, X. Zhang, R. Zhang, L. Zhou, X. Yan, M. Wang, X. Hou, Y. Cao, Antibacterial evaporator based on reduced graphene oxide/polypyrrole aerogel for solar-driven desalination, Nano Research (2022). https://doi.org/10.1007/s12274-021-4041-4.

[15] J. Abdi, A.J. Sisi, M. Hadipoor, A. Khataee, State of the art on the ultrasonic-assisted removal of environmental pollutants using metal-organic frameworks, J. Hazard. Mater. 424 (2022) 127558. https://doi.org/https://doi.org/10.1016/j.jhazmat.2021.127558.

[16] Z. Li, X. Ma, D. Chen, X. Wan, X. Wang, Z. Fang, X. Peng, Polyaniline-Coated MOFs Nanorod Arrays for Efficient Evaporation-Driven Electricity Generation and Solar Steam Desalination, Advanced Science 8(7) (2021) 2004552. https://doi.org/https://doi.org/10.1002/advs.202004552.

[17] A. Allahbakhsh, Z. Jarrahi, G. Farzi, A. Shavandi, Three-dimensional nanoporous Cu-BTC/graphene oxide nanocomposites with engineered antibacterial properties synthesized via a one-pot solvosonication process, Mater. Chem. Phys. 277 (2022) 125502. https://doi.org/10.1016/j.matchemphys.2021.125502.

[18] B. Pratap, S. Kumar, S. Nand, I. Azad, R.N. Bharagava, L.F. Romanholo Ferreira, V. Dutta, Wastewater generation and treatment by various eco-friendly technologies: Possible health hazards and further reuse for environmental safety, Chemosphere 313 (2023) 137547. https://doi.org/10.1016/j.chemosphere.2022.137547.

[19] C.-R. Zhang, W.-R. Cui, C.-P. Niu, S.-M. Yi, R.-P. Liang, J.-X. Qi, X.-J. Chen, W. Jiang, L. Zhang, J.-D. Qiu, rGO-based covalent organic framework hydrogel for synergistically enhance uranium capture capacity through photothermal desalination, Chemical Engineering Journal 428 (2022) 131178. https://doi.org/10.1016/j.cej.2021.131178.

[20] N. Nazari, A. Allahbakhsh, A.R. Bahramian, Analytical effective thermal conductivity model for colloidal porous composites and nanocomposites based on novolac/graphene oxide aerogels, International Journal of Energy Research 46(12) (2022) 16608-16628. https://doi.org/10.1002/er.8323.

[21] M.S. Irshad, X. Wang, M.S. Abbasi, N. Arshad, Z. Chen, Z. Guo, L. Yu, J. Qian, J. You, T. Mei, Semiconductive, Flexible MnO2 NWs/Chitosan Hydrogels for Efficient Solar Steam

Generation, ACS Sustainable Chemistry & Engineering 9(10) (2021) 3887-3900. https://doi.org/10.1021/acssuschemeng.0c08981.

[22] J. Zhang, Z. Li, T. Meng, S. Zang, C. Yang, X. Luo, H. Wang, J. Chen, F. Jing, C. Wang, H. Xu, Y. Zhou, Monolithic all-weather solar-thermal interfacial membrane evaporator, Chemical Engineering Journal 450 (2022). https://doi.org/10.1016/j.cej.2022.137893.

[23] R. Jayawardena, D.S. Eldridge, F. Malherbe, Sonochemical synthesis of improved graphene oxide for enhanced adsorption of methylene blue, Colloids and Surfaces A: Physicochemical and Engineering Aspects 650 (2022) 129587. https://doi.org/10.1016/j.colsurfa.2022.129587.

[24] A. Allahbakhsh, A.R. Bahramian, Novolac-derived carbon aerogels pyrolyzed at high temperatures: experimental and theoretical studies, RSC Advances 6(76) (2016) 72777-72790. https://doi.org/10.1039/c6ra12947a.

[25] A. Allahbakhsh, PVC/rice straw/SDBS-modified graphene oxide sustainable Nanocomposites: Melt mixing process and electrical insulation characteristics, Composites Part A: Applied Science and Manufacturing 134 (2020) 105902. https://doi.org/10.1016/j.compositesa.2020.105902.

[26] M. Khalaj, A. Allahbakhsh, A.R. Bahramian, A. Sharif, Structural, mechanical and thermal behaviors of novolac/graphene oxide nanocomposite aerogels, J. Non-Cryst. Solids 460 (2017) 19-28. https://doi.org/10.1016/j.jnoncrysol.2017.01.026.

[27] M. Acik, G. Lee, C. Mattevi, M. Chhowalla, K. Cho, Y.J. Chabal, Unusual infrared-absorption mechanism in thermally reduced graphene oxide, Nature Materials 9(10) (2010) 840-845. https://doi.org/10.1038/nmat2858.

[28] A. Allahbakhsh, S. Yari, M. Safari, D.P. Dubal, Poly(ethylene disulfide)/graphene oxide nanocomposites: Dynamic-mechanical and electrochemical properties, Eur. Polym. J. 130 (2020) 109694. https://doi.org/10.1016/j.eurpolymj.2020.109694.

[29] H. Jian, Y. Wang, W. Li, Y. Ma, W. Wang, D. Yu, Reduced graphene oxide aerogel with the dual-cross-linked framework for efficient solar steam evaporation, Colloids and Surfaces A: Physicochemical and Engineering Aspects 629 (2021) 127440. https://doi.org/10.1016/j.colsurfa.2021.127440.

[30] M. Acik, G. Lee, C. Mattevi, A. Pirkle, R.M. Wallace, M. Chhowalla, K. Cho, Y. Chabal, The Role of Oxygen during Thermal Reduction of Graphene Oxide Studied by Infrared Absorption Spectroscopy, The Journal of Physical Chemistry C 115(40) (2011) 19761-19781. https://doi.org/10.1021/jp2052618.

[31] C. Petit, J. Burress, T.J. Bandosz, The synthesis and characterization of copper-based metal–organic framework/graphite oxide composites, Carbon 49(2) (2011) 563-572. https://doi.org/10.1016/j.carbon.2010.09.059.

[32] J.-B. Wu, M.-L. Lin, X. Cong, H.-N. Liu, P.-H. Tan, Raman spectroscopy of graphene-based materials and its applications in related devices, Chem. Soc. Rev. 47(5) (2018) 1822-1873. https://doi.org/10.1039/c6cs00915h.

[33] D. López-Díaz, M. López Holgado, J.L. García-Fierro, M.M. Velázquez, Evolution of the Raman Spectrum with the Chemical Composition of Graphene Oxide, The Journal of Physical Chemistry C 121(37) (2017) 20489-20497. https://doi.org/10.1021/acs.jpcc.7b06236.

[34] A. Allahbakhsh, A.R. Bahramian, Self-assembled and pyrolyzed carbon aerogels: an overview of their preparation mechanisms, properties and applications, Nanoscale 7(34) (2015) 14139-14158. https://doi.org/10.1039/c5nr03855c.

[35] M.S. Irshad, N. Arshad, X. Wang, H.R. Li, M.Q. Javed, Y. Xu, L.A. Alshahrani, T. Mei, J. Li, Intensifying Solar Interfacial Heat Accumulation for Clean Water Generation Excluding Heavy Metal Ions and Oil Emulsions, Solar RRL 5(11) (2021) 2100427. https://doi.org/10.1002/solr.202100427.

[36] M.S. Irshad, X. Wang, A. Abbas, F. Yu, J. Li, J. Wang, T. Mei, J. Qian, S. Wu, M.Q. Javed, Salt-resistant carbon dots modified solar steam system enhanced by chemical advection, Carbon 176 (2021) 313-326. https://doi.org/10.1016/j.carbon.2021.01.140.

[37] R.-P. Ye, L. Lin, C.-C. Chen, J.-X. Yang, F. Li, X. Zhang, D.-J. Li, Y.-Y. Qin, Z. Zhou, Y.-G. Yao, Synthesis of Robust MOF-Derived Cu/SiO2 Catalyst with Low Copper Loading via Sol–Gel Method for the Dimethyl Oxalate Hydrogenation Reaction, ACS Catal. 8(4) (2018) 3382-3394. https://doi.org/10.1021/acscatal.8b00501.

[38] M.S. Irshad, N. Arshad, J. Zhang, C. Song, N. Mushtaq, M. Alomar, T. Shamim, V.-D. Dao, H. Wang, X. Wang, H. Zhang, Wormlike Perovskite Oxide Coupled with Phase-Change Material for All-Weather Solar Evaporation and Thermal Storage Applications, Advanced Energy and Sustainability Research 4(3) (2023) 2200158. https://doi.org/10.1002/aesr.202200158.

[39] X. Han, L.V. Besteiro, C.S.L. Koh, H.K. Lee, I.Y. Phang, G.C. Phan-Quang, J.Y. Ng, H.Y.F. Sim, C.L. Lay, A. Govorov, X.Y. Ling, Intensifying Heat Using MOF-Isolated Graphene for Solar-Driven Seawater Desalination at 98% Solar-to-Thermal Efficiency, Advanced Functional Materials 31(13) (2021) 2008904. https://doi.org/10.1002/adfm.202008904.

[40] A. Tong, X. Tang, F. Zhang, B. Wang, Study on the shift of ultraviolet spectra in aqueous solution with variations of the solution concentration, Spectrochimica Acta Part A: Molecular and Biomolecular Spectroscopy 234 (2020) 118259. https://doi.org/10.1016/j.saa.2020.118259.

[41] K. Yang, G. Zhou, Q. Xu, The elasticity of MOFs under mechanical pressure, RSC Advances 6(44) (2016) 37506-37514. https://doi.org/10.1039/c5ra23149c.

[42] M. Berer, Z. Major, G. Pinter, D.M. Constantinescu, L. Marsavina, Investigation of the dynamic mechanical behavior of polyetheretherketone (PEEK) in the high stress tensile

regime, Mechanics of Time-Dependent Materials 18(4) (2013) 663-684. https://doi.org/10.1007/s11043-013-9211-7.

[43] Z. Bai, Q. Liu, H. Zhang, J. Liu, R. Chen, J. Yu, R. Li, P. Liu, J. Wang, Mussel-inspired anti-biofouling and robust hybrid nanocomposite hydrogel for uranium extraction from seawater, Journal of Hazardous Materials 381 (2020) 120984. https://doi.org/10.1016/j.jhazmat.2019.120984.

[44] B. Omran, K.-H. Baek, Graphene-derived antibacterial nanocomposites for water disinfection: Current and future perspectives, Environ. Pollut. 298 (2022) 118836. https://doi.org/10.1016/j.envpol.2022.118836.

[45] X. Ming, A. Guo, Q. Zhang, Z. Guo, F. Yu, B. Hou, Y. Wang, K.P. Homewood, X. Wang, 3D macroscopic graphene oxide/MXene architectures for multifunctional water purification, Carbon 167 (2020) 285-295. https://doi.org/10.1016/j.carbon.2020.06.023.